Materials Today Bio 32 (2025) 101740

Contents lists available at ScienceDirect

Materials Today Bio

journal homepage: www.journals.elsevier.com/materials-today-bio

3D bioprinted biomimetic MOF-functionalized hydrogel scaffolds for bone regeneration: Synergistic osteogenesis and osteoimmunomodulation

San-yang Yu [a], Ting Wu [a], Kai-hao Xu [a], Ru-yue Liu [a], Tian-hao Yu [b,*], Zhen-hua Wang [c,**], Zhong-ti Zhang [a,***]

[a] The VIP Department, School and Hospital of Stomatology, China Medical University, Shenyang, 110002, PR China
[b] The VIP Department, School and Hospital of Stomatology, China Medical University, Liaoning Provincial Key Laboratory of Oral Diseases, Shenyang, 110002, PR China
[c] Department of Physiology, School of Life Sciences, China Medical University, Shenyang, 110122, PR China

ARTICLE INFO

Keywords:
Bioprint
Hydrogel
Metal–organic frameworks
Osteogenesis
Bone regeneration

ABSTRACT

Critical-size bone defects remain a significant clinical challenge. The lack of endogenous stem cells with osteogenic differentiation potential in the defect area, combined with the inflammatory responses induced by scaffold implantation, highlights the need for biomaterials that can deliver stem cells and possess inflammatory regulation properties. In this study, we developed a 3D bioprinted gelatin methacrylate (GelMA) hydrogel scaffold modified with luteolin-loaded ZIF-8 (LUT@ZIF-8) nanoparticles, designed to deliver bone marrow mesenchymal stem cells (BMSCs) to the defect site and release bioactive components that promote osteogenesis and modulate the immune microenvironment. The LUT@ZIF-8/GelMA hydrogel scaffolds demonstrated excellent physical properties and biocompatibility. The sustained release of luteolin and zinc ions from the LUT@ZIF-8 nanoparticles conferred antibacterial, osteoinductive, and inflammatory regulation effects. The immune microenvironment modulated by LUT@ZIF-8/GelMA hydrogel scaffolds facilitated osteogenic differentiation of BMSCs. Furthermore, *in vivo* experiments confirmed the osteogenic and inflammatory regulation capabilities of the LUT@ZIF-8/GelMA hydrogel scaffolds. In conclusion, the 3D bioprinted LUT@ZIF-8/GelMA hydrogel scaffolds exhibit osteoimmunomodulatory properties, presenting a promising strategy for the treatment of bone defects.

1. Introduction

The management of critical-size bone defects (CSBDs) caused by tumors, trauma, or inflammation remains a significant challenge in clinical practice [1]. These defects exceed the bone's natural regenerative capacity, necessitating the use of additional interventions for effective treatment [2,3]. One of the primary obstacles to successful bone repair is the lack of endogenous stem cells at the defect site, which limits the regenerative potential of the tissue. To address this challenge, three-dimensional (3D) bioprinting has emerged as a promising strategy in tissue regeneration. By using biocompatible materials combined with cells and growth factors, 3D bioprinting allows for the precise fabrication of customized scaffolds with controlled pore structure, ensuring uniform cell distribution, efficient nutrient exchange, and enhanced cell growth and differentiation [4].

Biomaterial implantation triggers a complex immune response, which was once considered a barrier to the development of bone regenerative materials. Inflammation can limit the regenerative activity of stem cells, making it difficult to achieve optimal repair [5,6]. Traditional strategies have focused on designing bioinert materials to minimize immune responses. However, while these materials reduce immune activation, they also restrict the osteoinductive potential of the scaffolds, presenting a limitation in meeting clinical needs [7]. Recent advancements in osteoimmunology have shifted biomaterial research from immune evasion to immune reprogramming, focusing on the synergistic role of immunomodulatory functions in enhancing osteogenesis [8]. Bone formation, in fact, is the result of dynamic interactions between the skeletal and immune systems. Researchers are increasingly

* Corresponding author.
** Corresponding author.
*** Corresponding author.
E-mail addresses: yutianhao@hotmail.com (T.-h. Yu), wzhcmusl@163.com (Z.-h. Wang), ztzhang@cmu.edu.cn (Z.-t. Zhang).

https://doi.org/10.1016/j.mtbio.2025.101740
Received 3 February 2025; Received in revised form 30 March 2025; Accepted 6 April 2025
Available online 8 April 2025

recognizing the pivotal role of macrophages in coordinating bone metabolism [9,10]. Previous studies have shown that macrophages interact with mesenchymal stem cells and secrete a variety of bioactive molecules which play critical roles in promoting osteogenic differentiation [11]. Notably, macrophages exhibit remarkable plasticity, with their phenotypic and functional states being modulated by the local microenvironment. The surface morphology, physicochemical properties, and cytokine release capacity of biomaterials significantly influence immune-inflammatory responses [12]. This plasticity provides the opportunity to modulate macrophages through biomaterials, thereby establishing an immune microenvironment that supports bone regeneration.

Hydrogels, which can mimic the natural extracellular matrix, are particularly suitable for cell encapsulation [13–15]. Gelatin methacryloyl (GelMA) is a photosensitive hydrogel derived from gelatin that rapidly cross-links under ultraviolet (UV) light [16]. GelMA contains multiple arginine-glycine-aspartate motifs, which facilitate cell adhesion and proliferation, as well as matrix metalloproteinase recognition sites that promote cellular remodeling. These properties make it highly biocompatible and widely used in 3D printing tissue engineering scaffolds [17,18]. However, its limited mechanical strength and lack of osteogenic activity necessitate modifications to render it a suitable bioink for bone regeneration application [19]. Luteolin, a natural flavonoid found in various plants, has been shown to have multiple pharmacological properties, including antioxidant, antibacterial, osteogenesis, and anti-inflammatory activities [20–22]. It has been shown to influence macrophage polarization by promoting the transition from M1 phenotype to M2 phenotype [23,24]. Despite its therapeutic potential, the clinical use of luteolin is constrained by its low bioavailability, resulting from poor solubility and rapid metabolic clearance [25]. To address this, zeolitic imidazolate framework-8 (ZIF-8), a metal-organic framework composed of zinc ions (Zn^{2+}) and 2-methylimidazole ligands, has high porosity and large specific surface area, making it an efficient carrier for drug loading and controlled release [26–29]. The gradual degradation of ZIF-8 not only releases Zn^{2+} but also enables the sustained delivery of encapsulated drugs, which can maintain their bioactivity at appropriate concentrations [30–33].

In this study, we developed a bioprinted biomimetic hydrogel scaffold to address the multifaceted challenges of bone repair by combining antibacterial, osteogenic, and osteoimmunomodulatory properties and supporting stem cell delivery (Fig. 1). We synthesized luteolin-loaded ZIF-8 (LUT@ZIF-8) nanoparticles using a one-pot method and incorporated them into GelMA to create a functional bioink (LUT@ZIF-8/GelMA) for bioprinting. LUT@ZIF-8/GelMA hydrogel scaffolds mimic extracellular matrix properties and possess a porous structure that allows nutrient exchange, facilitating the delivery of bone marrow mesenchymal stem cells (BMSCs) to bone defect sites. The incorporation of LUT@ZIF-8 nanoparticles enables the hydrogel scaffolds to achieve sustained release of luteolin and Zn^{2+}, thereby synergistically promoting osteogenesis by enhancing BMSCs osteogenic differentiation and modulating the immune microenvironment. This study highlights the potential of LUT@ZIF-8/GelMA hydrogel scaffolds in enhancing bone regeneration, providing an innovative approach for clinical bone defect repair.

2. Materials and methods

2.1. Synthesis and characterization of LUT@ZIF-8 nanoparticles

2.1.1. Preparation of ZIF-8 and LUT@ZIF-8 nanoparticles

LUT@ZIF-8 nanoparticles were synthesized using the one-pot method as described previously [29,34]. In brief, a zinc nitrate hexahydrate (Aladdin, China) solution (100 mg in 5 mL deionized water) was mixed with 10 mL methanol solution containing 221 mg of 2-methylimidazole (Aladdin, China) and 5 mg of luteolin (Sigma, USA). The resulting mixture was stirred at 25°C for 15 min and aged for an additional 2 h. The precipitate was centrifugated, washed with methanol, and dried overnight. ZIF-8 nanoparticles were synthesized for control experiments

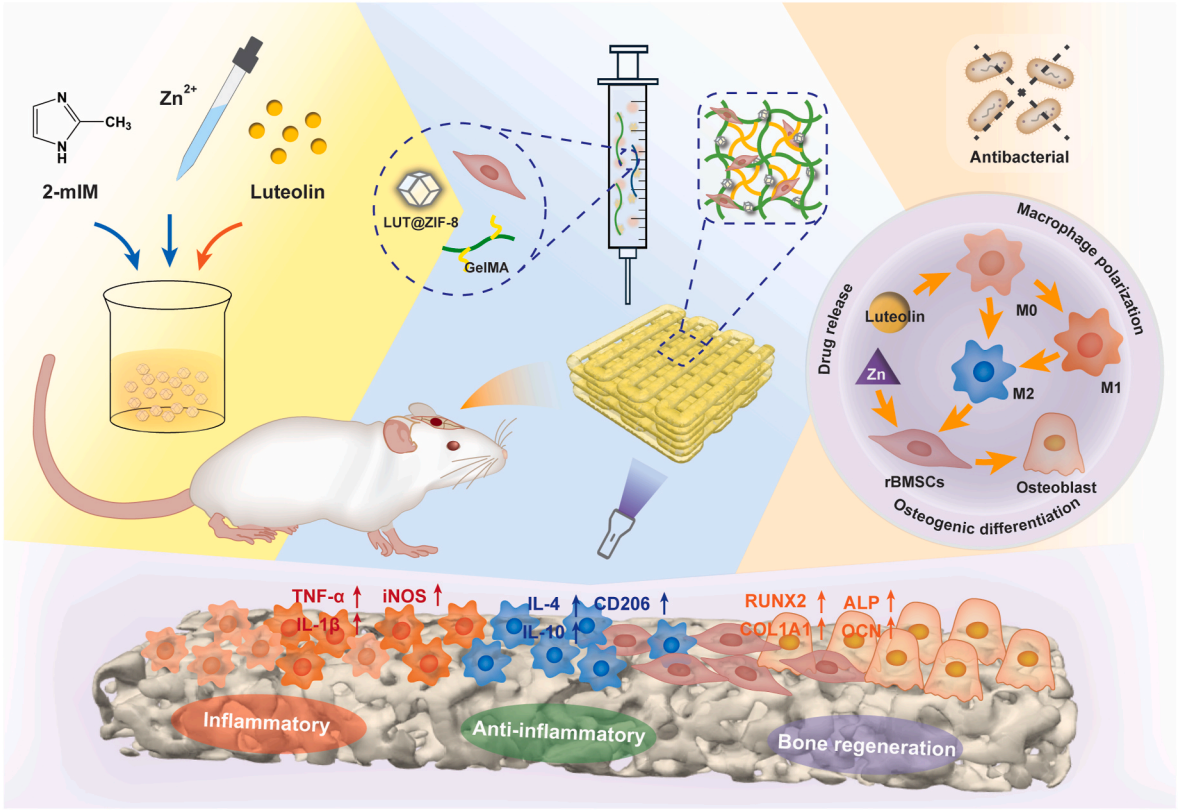

Fig. 1. Schematic illustration of LUT@ZIF-8/GelMA bioprinted scaffolds for bone regeneration.

following the procedure outlined in a prior study [29].

2.1.2. Characterization of ZIF-8 and LUT@ZIF-8 nanoparticles

The morphology of ZIF-8 and LUT@ZIF-8 nanoparticles was analyzed using transmission electron microscopy (TEM; FEI, USA), while energy dispersive spectroscopy (EDS) was employed to determine their elemental composition. X-ray diffraction (XRD; Bruker, USA) was used to examine the crystalline structure of both nanoparticles, and Fourier transform infrared spectroscopy (FTIR; Thermofisher, USA) was employed to identify the functional groups present. The zeta potential of ZIF-8, LUT@ZIF-8, and luteolin was measured to assess surface charge. Thermogravimetric analysis (TGA; NETZSCH, Germany) was performed to evaluate the thermal stability of ZIF-8 nanoparticles, luteolin, and LUT@ZIF-8 nanoparticles.

The drug loading capacity of LUT@ZIF-8 nanoparticles was assessed by dissolving the nanoparticles in 10 mL of 0.1 M hydrochloric acid. The solution of ZIF-8 and LUT@ZIF-8 nanoparticles was scanned from 200 to 900 nm using a UV–Vis spectrophotometer (YiPu, China). The luteolin solution was also analyzed within the same wavelength range to determine the maximum absorption wavelength. The absorbance of the solution of LUT@ZIF-8 nanoparticles (volume: V, mass of LUT@ZIF-8 nanoparticles: $m_{LUT@ZIF\text{-}8}$) was measured at the identified wavelength, and the luteolin concentration (C_{LUT}) was determined using a standard calibration curve. The drug loading capacity was calculated using the following formula:

$$Drug\ Loading\ Capacity\ (\%) = (C_{LUT} \times V)/m_{LUT@ZIF-8} \times 100\% \quad (1)$$

The drug release behavior of LUT@ZIF-8 nanoparticles was evaluated by incubating 10 mg of nanoparticles in 10 mL of PBS at 37°C with shaking at 100 rpm. At the specified time points (n), 2 mL of medium (V_e) was collected after centrifugation at 8000 rpm for 5 min and replaced with fresh PBS to maintain a total volume (V_0) of 10 mL. The supernatant's absorbance was measured via UV–Vis spectrophotometer, and the luteolin concentration (C_i) was quantified using the standard curve. The cumulative release percentage (E_r) was calculated based on the total luteolin mass (m_{LUT}) using the following formula:

$$E_r\ (\%) = \left(V_e \sum 1(n \hat{-} 1)C_i + V_o C_n\right) \Big/ m_{LUT} \times 100\% \quad (2)$$

2.2. Cell culture

Rat bone marrow mesenchymal stem cells were isolated from 4-week-old Sprague Dawley (SD) rats using established protocols [35]. The rBMSCs were cultured in α-MEM medium (Gibco, USA) supplemented with 10% fetal bovine serum (FBS; Sera-Pro, Germany) and 1% penicillin/streptomycin (P/S; YEASEN, China). Flow cytometry was employed to characterize the surface markers of rBMSCs. RAW 264.7 cells were sourced from Procell and cultured in RAW 264.7 specific culture medium (Procell, China) consisting of DMEM (glucose concentration: 25 mM), 10% FBS, and 1% P/S.

2.3. Fabrication and characterization of bioprinted scaffolds

2.3.1. 3D bioprinting of hydrogel scaffolds

LUT@ZIF-8/GelMA bioink was prepared as follows: 50 mg of lithium phenyl-2,4,6-trimethylbenzoylphosphonate (LAP; EFL, China) was dissolved in 10 mL of PBS and incubated at 45°C for 15 min with intermittent stirring. Subsequently, 500 mg of GelMA (EFL, China) was added to 5 mL of the prepared LAP solution and heated at 65°C in the dark for 15 min. After sterilization, the suspension of LUT@ZIF-8 nanoparticles was incorporated into the GelMA solution at a 1:1 (v/v) ratio, followed by ultrasonication for 5 min to form the LUT@ZIF-8/GelMA bioink. The bioinks were loaded into 5 mL screw-port syringes with 23 G needles and placed in a 3D bioprinter (Sunp, China). The syringe and platform temperature were set at 18–22°C and 18°C, respectively. The printing and extrusion speeds were set at 5 mm/min and 2 mm/min, respectively. UV curing was conducted at a wavelength of 405 nm with a light intensity of 0.5 W/cm^2. For bioprinting of hydrogel scaffolds encapsulating rBMSCs, rBMSCs were suspended in bioink at a density of 1.5 × 10^6 cells/mL.

To determine the optimal concentration of LUT@ZIF-8 nanoparticles within the hydrogel scaffolds, bioinks with varying nanoparticle loadings were evaluated. Cytotoxicity was evaluated by CCK-8 assay. Bioprinted scaffolds were cultured for 3 days and then incubated with CCK-8 reagent (Beyotime, China) at 37°C for 1 h, and measured using a microplate reader (Tecan, Switzerland).

Once the optimal concentration of LUT@ZIF-8 nanoparticles was identified, control bioinks were prepared, including GelMA, LUT/GelMA, and ZIF-8/GelMA, following the same procedure outlined above (Table S1).

2.3.2. Characterization of hydrogel scaffolds

After determining the optimal nanoparticle concentration, 3D-printed hydrogel scaffolds were prepared for material characterization tests. The scaffolds were freeze-dried and then sprayed with gold. Morphological analysis was conducted using scanning electron microscopy (SEM; FEI, USA).

The compressive strength of the hydrogel scaffolds was evaluated through uniaxial compression testing on a universal mechanical testing machine with a loading rate of 1 mm/min. The elastic modulus was calculated from the slope of the stress-strain curve in the elastic region. The stresses and strains at points A and B were denoted as σ_A, σ_B and ε_A, ε_B, respectively. The elastic modulus was determined using the following formula:

$$Elastic\ Modulus\ (kPa) = (\sigma_A - \sigma_B) / (\varepsilon_A - \varepsilon_B) \quad (3)$$

Hydrophilicity was assessed by measuring the water contact angle of the scaffolds using an optical contact angle system. A 4 μL droplet of deionized water was carefully applied to the surface of the cylindrical hydrogel, and the contact angle was recorded after capturing the droplet image.

To evaluate the swelling behavior, the bioprinted hydrogel scaffolds were freeze-dried, weighed, and immersed in PBS at 37°C. At predetermined intervals, the samples were removed and weighed until swelling equilibrium was achieved. The dry weight before immersion (W_0) and the swelling weight at each time point (W_t) were measured, and the hydrogel scaffold's swelling ratio was calculated using the following formula:

$$Swelling\ Ratio\ (\%) = (W_t - W_0) / W_0 \times 100\% \quad (4)$$

The degradability of the bioprinted scaffolds was assessed by measuring wet weight loss during incubation in a 20 μg/mL collagenase solution in PBS at 37°C with shaking at 100 rpm. Scaffolds were weighed at specific time points, with the initial weight recorded as W_0 and the weight at each time point as W_t. The degradation ratio was calculated using the following formula:

$$Degradation\ Ratio\ (\%) = (1 - W_t/W_0) \times 100\% \quad (5)$$

The release of luteolin from LUT@ZIF-8/GelMA hydrogel scaffolds was detected and analyzed according to the methods described in section 2.1.2.

2.4. Antibacterial property evaluation

The antibacterial properties of the hydrogel scaffolds were assessed using the following procedure. The hydrogel scaffolds were immersed in 5 mL suspensions of *E. coli* and *S. aureus* (1 × 10^6 CFU/mL) and incubated at 37°C for 24 h. After dilution, 100 μL of the suspension was plated onto LB agar plates and further incubated at 37°C for observation. The absorbance of the bacterial suspensions was then measured at 600

nm using UV–Vis spectrophotometer to evaluate the bacterial viability. After collecting the bacteria, the samples were washed with saline and stained using the LIVE/DEAD BacLight bacterial viability and counting kit (Thermofisher, USA) according to the manufacturer's instructions. Fluorescence images were captured using an inverted fluorescence microscope (Nikon, Japan).

2.5. Biocompatibility of bioprinted scaffolds

The bioprinted scaffolds with rBMSCs were cultured in α-MEM medium, and cell proliferation within the scaffolds were assessed using the CCK-8 assay on days 1, 3, and 5. In addition, live/dead cell staining was performed at the same time points. Cell morphology was evaluated on days 5 and 7 using TRITC-phalloidin/DAPI staining (Solarbio, China). After fixation, permeabilization, and staining, samples were imaged via confocal laser scanning microscopy (OLYMPUS, Japan). To evaluate the effect of the scaffolds on macrophage proliferation, RAW 264.7 cells were co-cultured with bioprinted scaffolds for 3 days, and CCK-8 assays were conducted as described above.

2.6. In vitro osteogenesis with bioprinted scaffolds

2.6.1. Osteogenic induction of bioprinted scaffolds

Pre-prepared bioinks containing rBMSCs were bioprinted using a 3D bioprinter. Following 2 days of incubation, the medium was changed to osteogenic differentiation medium, composed of the complete medium with the addition of β-Glycerophosphate (10 mM; Aladdin, China), ascorbic acid (284 μM; Aladdin, China), and dexamethasone (10 nM; Solarbio, China) [36]. The medium was refreshed every 2 days.

2.6.2. Evaluation of in vitro osteogenic differentiation

On days 7 and 14 of osteogenic induction, the bioprinted scaffolds were fixed with 4% paraformaldehyde solution (PFA; Beyotime, China) and stained for alkaline phosphatase (ALP) activity using the BCIP/NBT ALP kit (Beyotime, China) according to the protocol. For semi-quantitative ALP analysis, bioprinted scaffolds were lysed using GelMA lysis solution (EFL, China), followed by cell lysis using Western and IP lysis buffer (Beyotime, China). The supernatant was collected, and ALP activity was quantified using an ALP detection kit (Beyotime, China), following to the standard protocol. Calcium deposition was evaluated via alizarin red S (ARS) staining on day 21 of induction, using ARS solution (OriCell, China). Simultaneously, hydrogel scaffolds without rBMSCs were co-cultured with rBMSCs, and ALP and ARS staining were conducted after 7 and 21 days, respectively, and the results were quantitatively analyzed using ImageJ.

To further evaluate the osteogenic potential of the bioprinted scaffolds, the expression of osteogenesis-related genes was quantified on day 10 of induction by RT-qPCR. Bioprinted scaffolds were dissolved using GelMA lysis solution to collect rBMSCs, and total RNA was extracted using RNAiso Plus. RNA was reverse-transcribed into cDNA with the PrimeScript RT kit. RT-qPCR was performed using the SYBR Green RT-qPCR kit (TaKaRa, Japan) on a QuantStudio 7 Pro real-time PCR system (Applied Biosystems, USA). The expression of osteogenic genes, including *RUNX2*, *COL1A1*, *ALP*, and *OCN*, was analyzed. *β-actin* was used as a loading control. Primer sequences used for RT-qRCR are listed in Table S2. Western blot analysis was performed to evaluate the expression of osteogenic-related proteins (RUNX2 and ALP). Total protein was extracted with RIPA (Beyotime, China), and concentration measured using a BCA kit (Beyotime, China). Proteins were separated by SDS-PAGE (Beyotime, China), transferred to PVDF membranes (Beyotime, China), and blocked with 5% milk. Membranes were incubated with primary antibody (RUNX2 and ALP) and secondary antibodies (Bioss, China). Signals were detected using an ECL kit (Beyotime, China) and imaged. β-actin was used as a loading control.

2.7. Assessment of inflammatory modulation induced by hydrogel scaffolds

The ability of LUT@ZIF-8/GelMA hydrogel scaffolds to induce M2 macrophage polarization was evaluated using immunofluorescence (IF) staining. RAW 264.7 cells were stimulated with 100 ng/mL lipopolysaccharide (LPS; Sigma, USA) for 24 h, followed by co-culturing with hydrogel scaffolds for an additional 2 days. After fixation, blocking, and incubation with primary antibodies (iNOS or CD206; Proteintech, China), the cells were treated with appropriate secondary antibodies (Bioss, China). DAPI was used for counterstaining, and fluorescence images were acquired using a confocal microscope. Fluorescence intensity was quantified using ImageJ. Flow cytometry was performed to further assess the phenotypic changes in M1 macrophages. After the same LPS treatment and scaffold exposure, RAW 264.7 cells were Fc-blocked for 15 min, fixed with 4% PFA, and subsequently incubated with the iNOS primary antibody for 1 h. After secondary antibody incubation for 30 min, the cells were analyzed by flow cytometry. The gene expression of *TNF-α*, *IL-1β*, *IL-4*, and *IL-10* were quantified by RT-qPCR, following the procedure outlined in section 2.6.2. Primer sequences for RT-qPCR are provided in Table S3.

2.8. Inflammation-regulation-mediated osteogenic differentiation of rBMSCs induced by hydrogel scaffolds

2.8.1. Preparation of conditioned medium for osteogenic induction

Conditioned medium was prepared to simulate the immune microenvironment mediated by different hydrogel scaffolds. RAW 264.7 cells were first stimulated with LPS for 24 h, followed by co-culturing with the hydrogel scaffolds for an additional 48 h. After removal of the scaffolds, serum-free α-MEM was added to the system and incubated for 24 h. The supernatant was then collected and mixed with osteogenic differentiation medium in a 1:1 (*v/v*) ratio to generate the conditioned medium, which was used for culturing rBMSCs.

2.8.2. Induction of osteogenic differentiation in rBMSCs by conditioned medium

Osteogenic differentiation of rBMSCs was induced using the conditioned medium. Osteogenic differentiation was assessed by ALP, ARS staining, RT-qPCR and Western blot, as outlined in Section 2.6.

2.9. In vivo study

2.9.1. Construction of rat CSBDs and bioprinted scaffold implantation

All animal procedures were approved by the Animal Care and Use Committee of China Medical University (No: CMU20241783). The CSBD models were established to evaluate the *in vivo* inflammatory regulation and osteogenic effects of the LUT@ZIF-8/GelMA scaffold. Eight-week-old male SD rats were randomly assigned to 5 groups: Blank, GelMA, ZIF-8/GelMA, LUT/GelMA, and LUT@ZIF-8/GelMA. Anesthesia was induced using 2% isoflurane, and after disinfecting with povidone-iodine, a 5 mm diameter cranial bone defect was created with a circular debridement drill. Bioprinted scaffolds were then implanted into the bone defects, after which the skin was sutured, the wound was disinfected, and intraperitoneal antibiotics were administered postoperatively.

2.9.2. Evaluation of bone regeneration in vivo

After 8 weeks of post-surgery, the rats were euthanized, and the skulls were extracted and fixed in the 4% PFA. Microcomputed tomography (Micro-CT; Bruker, USA) scanning was performed on all samples. 3D reconstructions were generated, and bone volume (BV) and percent bone volume (BV/TV) were quantified to assess osteogenesis in the defect region. Cranial samples were then fixed in 4 % PFA, decalcified using 10% ethylenediaminetetraacetic acid (Beyotime, China), embedded in paraffin, and sectioned into 5 μm slices. The sections were

processed and stained following standard protocols using hematoxylin and eosin (H&E) and Masson's trichrome (Beyotime, China) for histological analysis. After deparaffinization and antigen retrieval, the slices were incubated overnight at 4°C with primary antibodies against RUNX2 and OPN (Bioss, China). The following day, sections were treated with a secondary antibody, stained with DAB (Bioss, China), counterstained with hematoxylin, mounted, and examined microscopically to assess osteogenic marker expression.

2.9.3. Immunofluorescence staining to evaluate inflammatory modulation

At 2 weeks post-surgery, rats were euthanized, and paraffin-embedded sections of the cranial bone defect area were prepared for IF staining. Tissue sections were dewaxed, rehydrated, and stained as described in section 2.7 to evaluate macrophage polarization.

2.9.4. Biosafety evaluation of bioprinted scaffolds

To evaluate the *in vivo* biocompatibility of the bioprinted scaffolds, tissues from the heart, liver, spleen, lungs, and kidneys were collected from rats in week 8. The samples were subjected to H&E staining, and histopathological analysis was performed to identify any adverse effects or signs of toxicity related to the implanted scaffolds.

2.10. Statistical analysis

Results are presented as the mean ± standard deviation. Statistical analyses were performed using GraphPad Prism 10.1.2 (GraphPad Software, USA). Data was analyzed using one-way analysis of variance. The significance levels were defined as follows: $*p < 0.05$, $**p < 0.01$, $***p < 0.001$.

3. Results and discussions

3.1. Characterization of ZIF-8 and LUT@ZIF-8 nanoparticles

ZIF-8 and LUT@ZIF-8 nanoparticles were successfully synthesized at room temperature (Fig. 2A). The suspension ZIF-8 nanoparticles appears milky white, while the suspension of LUT@ZIF-8 nanoparticles exhibits a distinct ginger-yellow color (Fig. 2B). TEM image showed that both ZIF-8 and LUT@ZIF-8 nanoparticles exhibited a homogeneous morphology and were nearly identical in shape, displaying a relatively uniform rhombic dodecahedral morphology (Fig. 2C). However, the particle size of LUT@ZIF-8 nanoparticles was larger than those of ZIF-8 nanoparticles and the edges of LUT@ZIF-8 nanoparticles appeared more blurred (Fig. 2D). Energy-dispersive X-ray (EDX) spectroscopy analysis revealed that the elemental compositions of both materials were almost identical (Fig. S1). Elemental mapping demonstrated the homogeneous distribution of Zn and other elements within the structure of LUT@ZIF-8 nanoparticles (Fig. 2E).

The crystalline structures of ZIF-8 nanoparticles, luteolin, and LUT@ZIF-8 nanoparticles were characterized by XRD. The XRD patterns of both nanoparticles were consistent with the simulated pattern for ZIF-8 (Fig. 2F), displaying characteristic diffraction peaks at 2θ values of 7.27°, 10.34°, 12.70°, 14.65°, 16.41°, and 18.00°, corresponding to the (011), (002), (112), (022), (013), and (222) planes of ZIF-8, respectively [37]. The XRD patterns of LUT@ZIF-8 nanoparticles did not show any characteristic peaks of the luteolin (Fig. S2). FTIR spectroscopy was used to analyze the chemical structures of ZIF-8 nanoparticles, luteolin, and LUT@ZIF-8 nanoparticles. The FTIR spectra of ZIF-8 and LUT@ZIF-8 nanoparticles showed characteristic peaks corresponding to ZIF-8 (Fig. 2G), including Zn-N stretching at 420 cm^{-1}, C-N stretching at 1144 cm^{-1} and 1308 cm^{-1}, C=N stretching at 1579 cm^{-1}, and C-H stretching at 2928 cm^{-1} and 3133 cm^{-1} [38]. The spectrum of LUT@ZIF-8 nanoparticles exhibited a reduction in peak intensities and slight shifts. Notably, the peaks at 1099 cm^{-1} and 1648 cm^{-1} were likely attributable to C-O and C=C stretching vibrations from luteolin and the peaks observed at 805 cm^{-1} and 1262 cm^{-1} were attributed to C-H and O-H stretching modes within the aromatic ring of luteolin (Fig. S3) [39]. XRD and FITR results suggested that luteolin is encapsulated within the structure of LUT@ZIF-8 nanoparticles, with minimal luteolin present on the surface of LUT@ZIF-8 nanoparticles. Zeta potential measurements revealed that the incorporation of luteolin, with its negative charge, decreased the zeta potential of ZIF-8 nanoparticles from 10.5 mV to −6.1 mV (Fig. 2H). Previous studies have indicated that negatively charged biomaterials can enhance osteogenic differentiation [40]. Additionally, these materials have been shown to modulate the immune microenvironment by stimulating macrophages to secrete anti-inflammatory cytokines [41].

Thermogravimetric analysis was performed to assess the thermal stability of ZIF-8 nanoparticles, luteolin, and LUT@ZIF-8 nanoparticles (Fig. 2I). All samples exhibited slight mass loss between 100°C and 200°C, likely due to moisture evaporation. ZIF-8 nanoparticles showed a significant reduction in mass, from 97.6% at 344 °C to 34% at 679°C. Luteolin displayed a marked weight decrease, from 97.3% at 289°C to 1.4% at 548°C. The greater mass loss observed for LUT@ZIF-8 nanoparticles compared to ZIF-8 nanoparticles is attributed to the decomposition of luteolin. Previous studies suggest that the hydroxyl groups in drug can coordinate with Zn^{2+} in ZIF-8 nanoparticles [42], potentially explaining the shift in degradation temperature and the relatively smaller mass loss observed for LUT@ZIF-8 nanoparticles at earlier stages. Luteolin loading efficiency was determined using UV–Vis spectrophotometer. After acid treatment, LUT@ZIF-8 nanoparticles displayed distinct absorption peaks at 264 nm and 346 nm (Fig. 2J), corresponding to the characteristic absorption of luteolin (Fig. S4), indicating that luteolin has been successful encapsulated within the ZIF-8 structure. The luteolin concentration in the solution was quantified using a standard calibration curve for luteolin: $Y = 0.02663 + 0.03505X$ (Fig. S5). The drug loading capacity was determined to be 16.72%. The degradation of ZIF-8 nanoparticles demonstrates pH sensitivity, remaining stable at neutral pH while accelerating under acidic conditions [43]. Fig. 2K presents the drug release profiles of LUT@ZIF-8 nanoparticles at different pH levels. Under acidic conditions, luteolin release from LUT@ZIF-8 nanoparticles is predominantly concentrated within the first 24 h, suggesting that ZIF-8 nanoparticles undergo rapid degradation in low pH environments, thus making acidic conditions an efficient trigger for drug release. In contrast, under neutral conditions, the drug release remains relatively stable. However, previous studies have demonstrated that even under neutral pH, the complex milieu of bodily fluids can accelerate the degradation of ZIF-8 nanoparticles. To improve retention at bone defect sites and optimize drug release dynamics, ZIF-8 nanoparticles are often integrated into hydrogel [32].

3.2. Characterization of hydrogel scaffolds

For effective bone regeneration, bioprinted scaffolds must exhibit appropriate mechanical strength, degradability, and biocompatibility. In this study, a GelMA bioink incorporating LUT@ZIF-8 nanoparticles was designed to enhance the performance of bioprinted scaffolds (Fig. 3A).

Flow cytometry was used to identify rBMSCs (Fig. S6), and the cell morphology was observed with a microscope (Fig. S7). To assess cell viability, we evaluated bioprinted scaffolds loaded with rBMSCs at varying concentrations of LUT@ZIF-8 nanoparticles using the CCK-8 assay. As shown in Fig. 3B, cell viability significantly decreased when the concentration of LUT@ZIF-8 nanoparticles exceeded 0.04%. Consequently, the 0.04% LUT@ZIF-8 nanoparticles concentration was selected for subsequent experiments.

Before photo-crosslinking, the LUT@ZIF-8/GelMA bioink displayed excellent plasticity, whereas, after photo-crosslinking, it gelled to form a stable structure (Fig. 3C). As shown in Fig. 3D, the LUT@ZIF-8/GelMA bioink demonstrated excellent printability. GelMA, ZIF-8/GelMA, LUT/GelMA, and LUT@ZIF-8/GelMA hydrogel scaffolds were

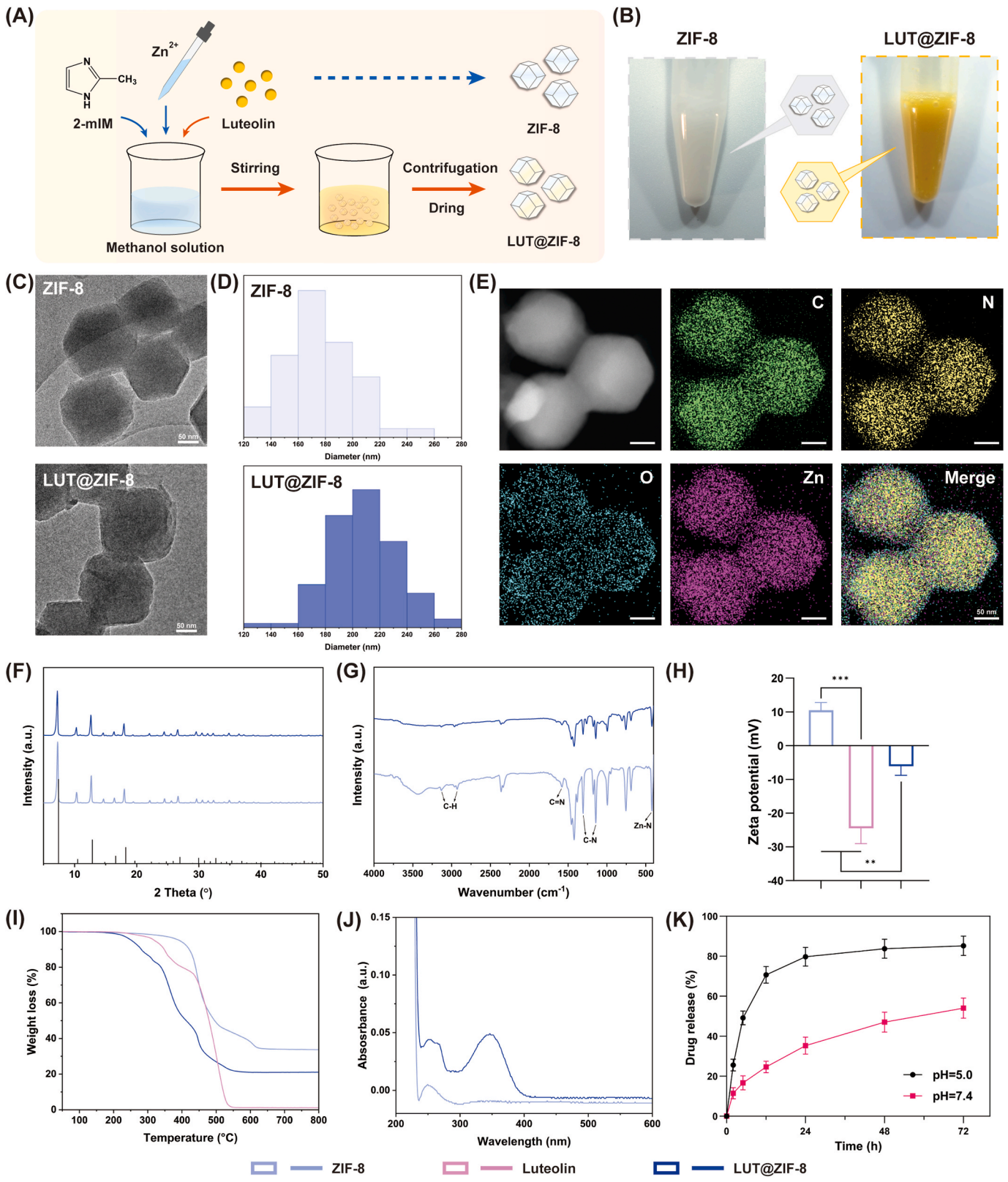

Fig. 2. Characterization of ZIF-8 and LUT@ZIF-8 nanoparticles. (A) Schematic illustration of the synthesis process for ZIF-8 and LUT@ZIF-8 nanoparticles. (B) Visual appearance of the suspensions of ZIF-8 and LUT@ZIF-8 nanoparticles. (C) Transmission electron microscopy images showing the morphology of ZIF-8 and LUT@ZIF-8 nanoparticles. (D) Particle size distribution of ZIF-8 and LUT@ZIF-8 nanoparticles. (E) EDX elemental mapping of LUT@ZIF-8 nanoparticles. (F) X-ray diffraction patterns of ZIF-8 and LUT@ZIF-8 nanoparticles. (G) Fourier-transform infrared spectra of ZIF-8 and LUT@ZIF-8 nanoparticles. (H) Zeta potential measurements of ZIF-8, LUT@ZIF-8 nanoparticles, and luteolin. (I) Thermogravimetric analysis profiles of ZIF-8 and LUT@ZIF-8 nanoparticles. (J) UV–vis spectra of acid-treated solution of ZIF-8 and LUT@ZIF-8 nanoparticles. (K) Drug release profile of LUT@ZIF-8 nanoparticles under different pH conditions.

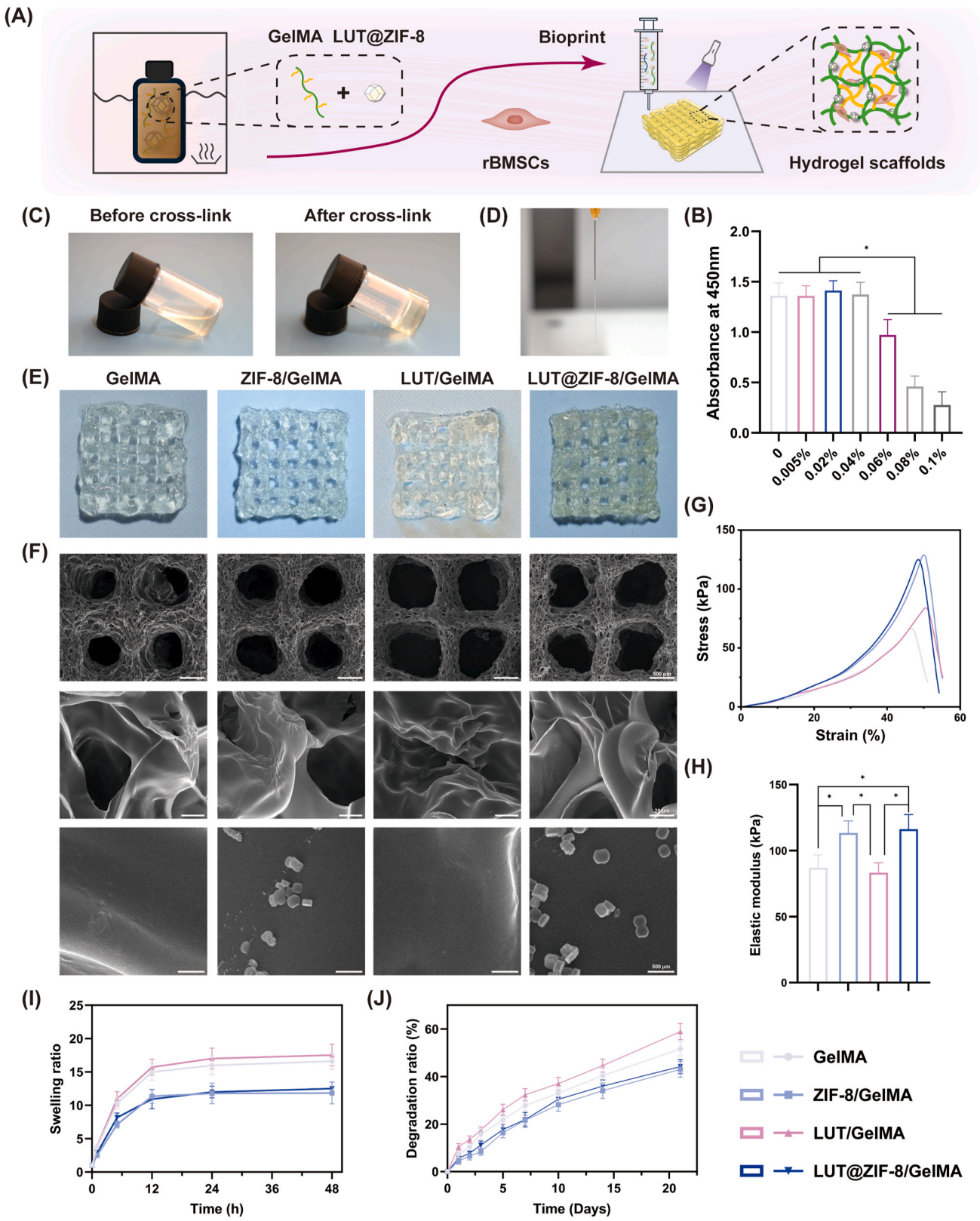

Fig. 3. Characterization of hydrogel scaffolds. (A) Schematic illustration of the bioprinting process of hydrogel scaffolds. (B) CCK-8 assay assessing cell viability in bioprinted scaffolds with varying concentrations of LUT@ZIF-8 nanoparticles. (C) Images of LUT@ZIF-8/GelMA bioink before and after photo-crosslinking. (D) Printability of the LUT@ZIF-8/GelMA bioink. (E) Digital images of hydrogel scaffolds. (F) Scanning electron microscopy images of hydrogel scaffolds. (G) Stress-strain curve of hydrogel scaffolds. (H) Elastic modulus of hydrogel scaffolds. (I) Swelling behavior of hydrogel scaffolds over time. (J) Degradation ratio of hydrogel scaffolds following collagenase treatment.

fabricated via 3D bioprinting (Fig. 3E). SEM images of freeze-dried scaffolds revealed a regular grid-like structure with abundant pores in all groups (Fig. 3F). The 3D-printed scaffolds formed macropores, with numerous smaller pores distributed across their surface, promoting nutrient transport and supporting cell proliferation [44]. Additionally, high-magnification SEM images demonstrated the distribution of ZIF-8 and LUT@ZIF-8 nanoparticles within the hydrogel matrix, showing that the nanoparticles were uniformly embedded and well-dispersed within the hydrogel network (Fig. 3F). Hydrophilicity tests indicated that all groups exhibited favorable water absorption properties (Fig. S8). Previous studies have shown that hydrophilic materials promote the secretion of anti-inflammatory cytokines by macrophages [45].

Adequate mechanical properties help maintain the scaffold's shape and prevent structural damage, which is essential the continuous repair of the bone defect area. The stress-strain curves of the hydrogel scaffolds of each group are presented in Fig. 3G. The ZIF-8/GelMA and LUT@ZIF-

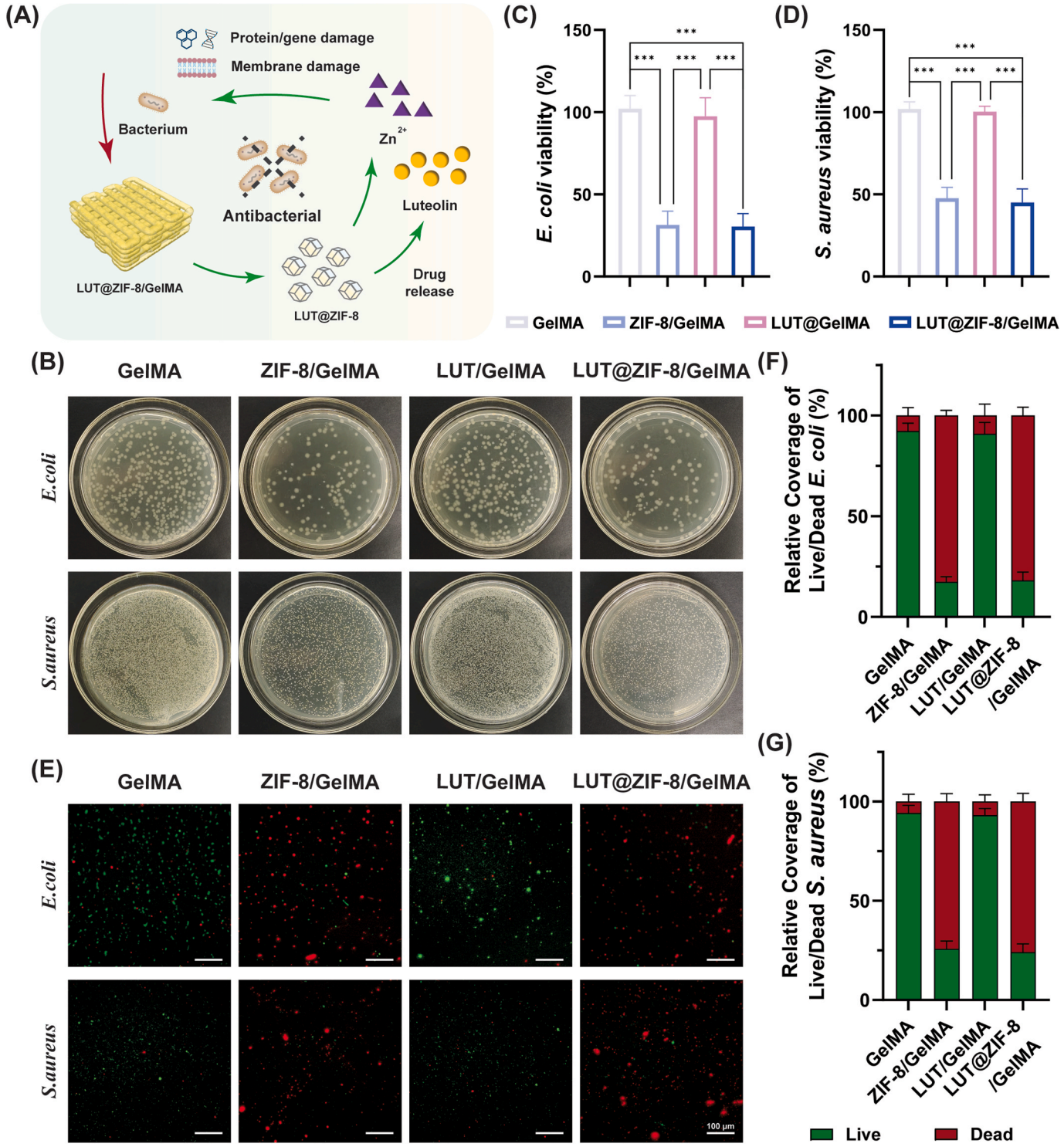

Fig. 4. Antibacterial activity and biocompatibility of hydrogel scaffolds. (A) Schematic illustration of the antibacterial process of the hydrogel scaffolds. (B) Colony formation of *E. coli* and *S. aureus*. (C) Viability of *E. coli*. (D) Viability of *S. aureus*. (E) Live/dead staining of *E. coli* and *S. aureus*. (F) Quantitative analysis of live/dead staining of *E. coli*. (G) Quantitative analysis of live/dead staining of *S. aureus*.

8/GelMA groups demonstrated increased elastic modulus compared to GelMA and LUT/GelMA groups (Fig. 3H). The reduced mechanical properties observed in the LUT/GelMA group may be partly due to the presence of luteolin, which potentially diminishes the crosslinking efficiency during the photo-crosslinking process. The swelling ratio, a key physical property of hydrogel scaffolds, plays an essential role in nutrient exchange and cell survival. However, excessive swelling may compromise scaffold shape and mechanical stability [42,46,47]. As shown in Fig. 3I, all groups exhibited rapid swelling and different rate in the first 5 h after immersion, then with a slower swelling rate, reaching equilibrium at 24 h. The swelling ratio of the ZIF-8/GelMA and LUT@ZIF-8/GelMA groups lower than that of the GelMA and LUT/-GelMA groups (Fig. S9). The degradation results showed that the degradation rate of ZIF-8/GelMA and LUT@ZIF-8/GelMA hydrogel scaffolds was relatively low, while the LUT/GelMA group exhibited a faster degradation rate (Fig. 3J). This may be due to luteolin reducing the photocrosslinking strength of the GelMA hydrogel. The hydrogel scaffolds exhibit appropriate biodegradability, providing ample space for cells and tissue ingrowth in the bone defect area. The release of therapeutic agents from hydrogel scaffolds is pivotal in modulating the immune microenvironment of bone defect sites. The drug release profile of the LUT@ZIF-8/GelMA hydrogel scaffolds revealed sustained luteolin release in PBS over 14 days (Fig. S10). Encapsulation of LUT@ZIF-8 nanoparticles within the GelMA matrix attenuated its degradation rate, thereby enabling prolonged and controlled release of the drug, a feature crucial for effective inflammatory modulation and tissue regeneration.

3.3. Antibacterial properties of hydrogel scaffolds

Infections commonly complicate bone defects, significantly impairing the healing process and diminishing treatment efficacy.

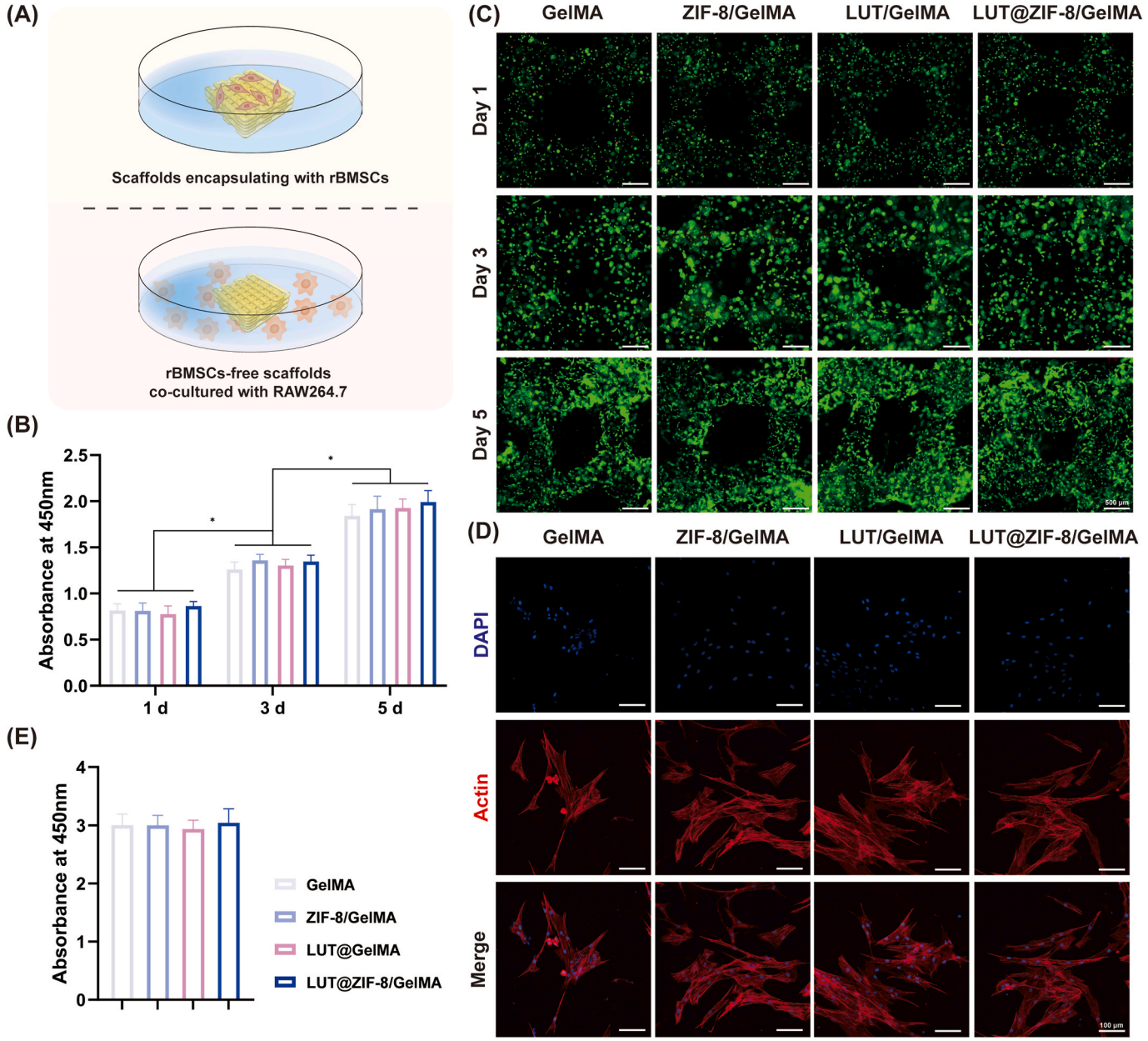

Fig. 5. Biocompatibility of hydrogel scaffolds. (A) Schematic illustration of the biocompatibility testing of hydrogel scaffolds. (B) CCK-8 assay of bioprinted scaffolds on days 1, 3 and 5. (C) Live/dead cell stainng of bioprinted scaffolds on days 1, 3 and 5. (D) TRITC/DAPI staining of bioprinted scaffolds on day 5. (E) CCK-8 assay of hydrogel scaffolds in co-culture with RAW 264.7 cells.

Consequently, developing biomaterials with antibacterial properties is crucial for preventing and managing bone infections [48]. To evaluate the antibacterial performance of the hydrogel scaffolds, antibacterial assays were performed against *E. coli* and *S. aureus* (Fig. 4A). Colony count analyses revealed that both the LUT@ZIF-8/GelMA and ZIF-8/GelMA groups significantly reduced colony counts, while the LUT/GelMA group showed minimal changes (Fig. 4B). After 24 h, the bacterial viability in the ZIF-8/GelMA and LUT@ZIF-8/GelMA groups significantly decreased (Fig. 4C–D). The live/dead staining images of *E. coli* and *S. aureus* are shown in Fig. 4E. The GelMA group mainly exhibited green fluorescence, indicating a high proportion of live bacteria. In contrast, the ZIF-8/GelMA group and the LUT@ZIF-8/GelMA group showed a significant amount of red fluorescence, suggesting that most bacteria had lost viability. The quantitative results of the live/dead bacterial staining demonstrated that the LUT@ZIF-8/GelMA hydrogel scaffold effectively inhibited bacterial growth (Fig. 4F–G).

These findings suggests that the LUT@ZIF-8/GelMA hydrogel scaffold possesses significant antibacterial activity, likely attributable to the combined release of luteolin and Zn^{2+}. The antibacterial properties of Zn^{2+} have been well documented, including its ability to disrupt bacterial cell membranes, leading to cellular damage [49,50]. Additionally, luteolin has been reported to inhibit DNA topoisomerases I and II, thereby impairing bacterial nucleic acid and protein synthesis [51,52]. In our study, the limited antibacterial effect of the LUT/GelMA group is likely due to the relatively low concentration of luteolin within the hydrogel scaffold.

3.4. Biocompatibility and cytotoxicity of bioprinted scaffolds

Bioprinted scaffolds loaded with rBMSCs were fabricated via bioprinting to evaluate their encapsulation capability for stem cells. In parallel, hydrogel scaffolds without rBMSCs were also prepared to assess their impact on macrophage proliferation (Fig. 5A).

Cell proliferation in different groups was evaluated by measuring cell viability at multiple time points using the CCK-8 assay. As shown in Fig. 5B, cell proliferation increased over time, with significant growth observed on days 1, 3, and 5. Live/dead staining further confirmed that cells were uniformly distributed within the scaffolds, with the majority of cells remaining viable (Fig. 5C). On day 5, TRITC-phalloidin staining revealed that rBMSCs extended in all scaffold groups, with more pronounced cell spreading observed in the LUT@ZIF-8/GelMA group compared to the GelMA group, indicating that LUT@ZIF-8/GelMA enhances cell extension (Fig. 5D). TRITC-phalloidin staining on day 7 showed that all groups supported cell extension, indicating that the hydrogel matrix successfully mimics the characteristics of the extracellular matrix, providing a favorable microenvironment for cell adhesion and spreading (Fig. S11). To evaluate the scaffolds' effect on macrophage proliferation, a CCK-8 assay was performed with RAW 264.7 cells. The results indicated that after 3 days, no noticeable cytotoxicity was observed in any of the scaffolds (Fig. 5E).

These findings demonstrate that all groups exhibited excellent cytocompatibility. The appropriate concentrations of LUT@ZIF-8 nanoparticles did not compromise the biocompatibility of the bioink. The rBMSCs within the bioprinted hydrogel scaffolds were able to proliferate and extend, and the hydrogel scaffolds did not hinder the proliferation of RAW 264.7 cells.

3.5. In vitro osteogenesis with bioprinted scaffolds

Bone marrow mesenchymal stem cells play a pivotal role in bone homeostasis and tissue regeneration, serving as essential seed cells in tissue engineering. BMSCs can directly osteogenic differentiation while also promoting tissue repair through paracrine signaling pathways [53]. However, bone defect areas often lack sufficient endogenous mesenchymal stem cells, making tissue regeneration challenging. Compared to acellular bone fillers, introducing exogenous BMSCs into bone defect sites via scaffolds loaded with rBMSCs significantly enhances bone regeneration outcomes [54]. Additionally, biomaterials used in bone tissue engineering should possess bioactivity that promotes BMSCs osteogenic differentiation. To assess the osteogenesis-promoting effect of hydrogel scaffolds, a series of experiments were conducted (Fig. 6A).

Alkaline phosphatase is critical in bone formation, as it hydrolyzes phosphates to release phosphoric acid for hydroxyapatite synthesis and degrades pyrophosphate, thereby alleviating its inhibitory effect on bone mineralization, thus promoting osteogenic differentiation [55]. ALP activity reflects the differentiation level of osteogenesis, and the *in vitro* osteogenic potential of the bioprinted scaffolds was evaluated through ALP staining and semi-quantitative analysis. ALP staining results revealed more intense staining in the LUT@ZIF-8/GelMA group compared to the other groups (Fig. 6B). This was corroborated by semi-quantitative analysis of ALP activity, which confirmed a significant increase in ALP activity in the LUT@ZIF-8/GelMA group (Fig. 6C–D). Additionally, ALP staining of rBMSCs co-cultured with hydrogel scaffolds further supported this finding (Fig. S12). Co-culturing rBMSCs with various hydrogel scaffolds under osteogenic induction for 21 days, ARS staining and quantitative analysis revealed that the LUT@ZIF-8/GelMA group exhibited the highest density of mineralized nodules, indicating its superior ability to promote mineralization (Fig. 6E–F). The ARS staining results of rBMSCs loaded in the bioprinted scaffolds were consistent with these findings (Fig. S13). RT-qPCR analysis of osteogenic gene expression after 10 days of induction demonstrated significantly higher gene expression of *RUNX2*, *COL1A1*, *ALP*, and *OCN* in the LUT@ZIF-8/GelMA group compared to other groups, indicating enhanced osteogenic activity (Fig. 6G–J). ZIF-8/GelMA and LUT/GelMA groups exhibited comparable trends, although their effects were weaker compared to the LUT@ZIF-8/GelMA group. The results of Western blot showed that the expression of osteogenesis-related proteins RUNX2 and ALP were significantly elevated in the LUT@ZIF-8/GelMA group compared with the other groups (Fig. 6K–M).

These results underscore the ability of the LUT@ZIF-8/GelMA hydrogel scaffold to promote osteogenic differentiation of BMSCs. Flavonoids, known for their unique chemical structures and biological activities, are widely recognized for stimulating osteogenesis [56]. Previous studies have shown that luteolin enhances ALP activity and collagen synthesis in osteoblasts, thereby promoting mineralization, with the Wnt signaling pathway implicated in this process [57,58]. Our findings further confirm the potential of luteolin in bone regeneration applications. Moreover, low concentrations of Zn^{2+} have been shown to promote the BMSCs osteogenic differentiation via the TGF-β and PI3K-AKT signaling pathways, while excessive concentrations of Zn^{2+} can induce apoptosis [8]. The gradual degradation of ZIF-8 nanoparticles encapsulated within the hydrogel facilitates the controlled release of Zn^{2+}, effectively maintaining optimal ion concentrations. In this study, the synergistic release of luteolin and Zn^{2+} from LUT@ZIF-8/GelMA bioprinted scaffolds contributes to the enhanced osteogenic effects observed.

3.6. Regulation of macrophage polarization by hydrogel scaffolds

The implantation of biomaterials into bone defects elicits a foreign body reaction, with macrophages playing a central role in this response [59,60]. M1 macrophages are crucial for pathogen clearance and the removal of necrotic tissue, in addition to their role in degrading and phagocytizing biological materials [61,62]. M2 macrophages are involved in tissue healing and regeneration [63,64]. As the first responders to bone biomaterials, macrophages exhibit remarkable plasticity, making inflammatory modulation a promising approach to enhance bone healing. The physicochemical properties and bioactive components of biomaterials dictate the functional state of macrophages [7]. Recent studies on biodegradable biomaterials for tissue regeneration have increasingly focused on promoting the polarization of macrophages from the pro-inflammatory M1 phenotype to the reparative M2

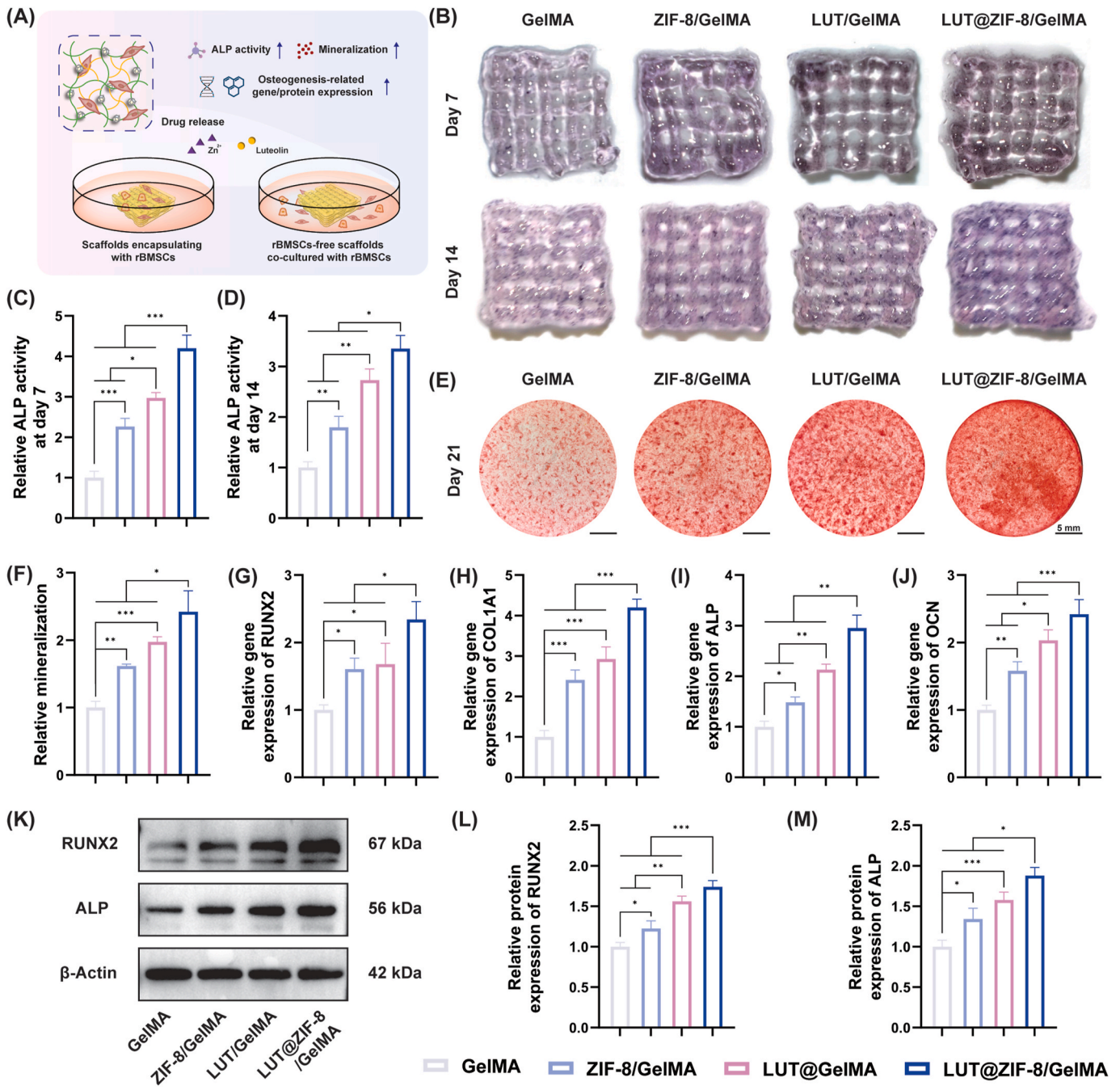

Fig. 6. The osteogenic properties of hydrogel scaffolds *in vitro*. (A) Schematic illustration of osteogenic differentiation promoted by hydrogel scaffolds.(B) Alkaline phosphatase (ALP) staining after 7 and 14 days of osteogenic induction. (C,D) Semi-quantitative analysis of ALP activity. (E) Alizarin red S staining (ARS) staining after 21 days of osteogenic induction in co-culture with rBMSCs-free hydrogel scaffolds (F) Quantitative analysis of ARS staining. (G–J) RT-qPCR analysis for osteogenic gene expression after 10 days of induction. (K) Western blot analysis of osteogenesis-related proteins expression after 10 days of induction. (L,M) Quantification of osteogenesis-related proteins expression levels.

phenotype [65–67]. To evaluate the inflammatory regulation effects of the LUT@ZIF-8/GelMA hydrogel scaffolds, a series of experiments were conducted (Fig. 7A).

iNOS is a typically associated with M1 macrophages, whereas CD206 is commonly used to identify M2 macrophages [68]. IF staining revealed that the LUT@ZIF-8/GelMA hydrogel scaffold effectively suppressed iNOS expression while enhancing CD206 expression, indicating a shift from the M1 to the M2 macrophage phenotype (Fig. 7B). Quantitative analysis of the IF staining further confirmed this shift (Fig. 7C). These findings were corroborated by flow cytometry, which showed a reduction in iNOS-positive cells in the LUT@ZIF-8/GelMA group compared to the other groups, suggesting a decrease in M1 macrophages (Fig. 7E–F). To further explore the inflammatory regulation properties of the scaffolds, RT-qPCR was performed to assess gene expression in RAW 264.7 cells. The results demonstrated that the LUT@ZIF-8/GelMA group significantly downregulated the expression of M1-associated pro-inflammatory cytokines, including *TNF-α* and *IL-1β*, while upregulating the expression of M2-related anti-inflammatory markers such as *IL-4* and *IL-10*. (Fig. 7G–J). Additionally, the ZIF-8/GelMA and LUT/GelMA groups influenced macrophage polarization in a similar trend to the LUT@ZIF-8/GelMA group, although to a lesser extent.

These findings confirmed that LUT@ZIF-8/GelMA hydrogel scaffolds

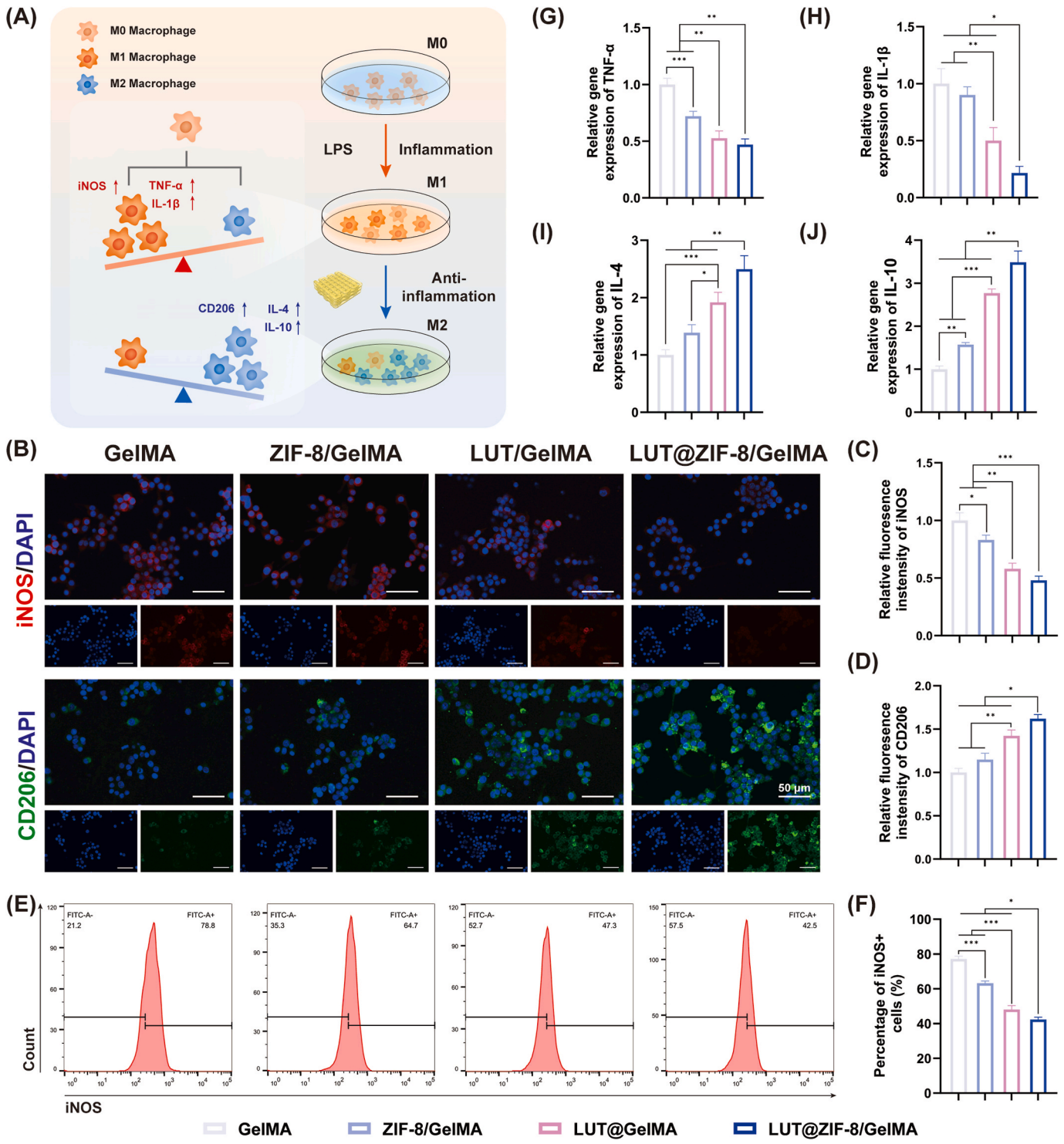

Fig. 7. Regulation of macrophage polarization by hydrogel scaffolds. (A) Schematic illustration of macrophage polarization induced by hydrogel scaffolds. (B) Immunofluorescent staining of iNOS and CD206. (C,D) Quantitative analysis of immunofluorescence staining. (E) Flow cytometry analysis of iNOS-positive cells. (G–J) Relative mRNA expression of M1-and M2-associated macrophage markers.

effectively regulate macrophage polarization, promoting the M2 phenotype. Previous studies have demonstrated that luteolin induces M2 polarization, suppressing inflammation through the modulation of p-STAT3 and p-STAT6 signaling [24]. Additionally, luteolin has been reported to inhibit osteoclast differentiation in macrophages, further emphasizing its role in inflammatory regulation and bone remodeling [69]. The degradation of ZIF-8 nanoparticles also releases Zn^{2+}, which are known to influence macrophage polarization [70]. In this study, the combined release of luteolin and Zn^{2+} from the LUT@ZIF-8/GelMA hydrogel scaffolds synergistically induced M2 macrophage polarization, created an anti-inflammatory immune microenvironment and highlighted the scaffold's strong inflammatory regulation properties.

3.7. Osteogenic differentiation mediated by inflammatory regulation

The intricate interplay between the skeletal and immune systems has

fueled the emergence and rapid progress of osteoimmunology. Macrophages play a pivotal role in initiating and enhancing bone repair by supporting the formation of bone callus. Transgenic mice that induce macrophage apoptosis show complete loss of bone formation due to macrophage depletion. Studies have shown that macrophages influence osteogenic differentiation of MSCs through direct contact with osteogenic cells and secreting growth factors and exosomes [71,72]. Therefore, the inflammatory regulation effects of biomaterials at the implantation site are critical to the success of bone regeneration [11]. To assess whether inflammatory regulation of RAW 264.7 cells by LUT@ZIF-8/GelMA hydrogel scaffolds could promote osteogenic differentiation in rBMSCs, RAW 264.7 cells were exposed to LPS and hydrogel scaffolds from each group. Following treatment, the culture medium was replaced, and the supernatant was collected to prepare conditioned medium, which was then used to induce osteogenic differentiation in rBMSCs (Fig. 8A).

Alkaline phosphatase staining and ARS staining were utilized to assess the impact of hydrogel scaffolds on the osteogenic differentiation of rBMSCs under inflammatory microenvironment stimulation. ALP staining after 7 and 14 days of treatment revealed that the LUT@ZIF-8/GelMA group exhibited higher ALP staining intensity compared to other groups, a finding confirmed by quantitative ALP staining analysis (Fig. 8B–D). After 21 days, ARS staining demonstrated a significantly greater density of mineralized nodules in the LUT@ZIF-8/GelMA group (Fig. 8E–F). ZIF-8/GelMA and LUT/GelMA groups exhibited similar trends to the LUT@ZIF-8/GelMA group, but the changes were weaker. The impact of hydrogel scaffolds on the osteogenic differentiation of rBMSCs under inflammatory microenvironment was evaluated at the genetic level using RT-qPCR. RT-qPCR analysis showed elevated expression of osteogenesis-related genes (*RUNX2*, *COL1A1*, *ALP*, and *OCN*) in the LUT@ZIF-8/GelMA group, relative to the other groups (Fig. 8G–J). The results of Western blot further confirmed this, showing significantly increased RUNX2 and ALP protein expression in the LUT@ZIF-8/GelMA group (Fig. 8K–M).

These results indicate that macrophage polarization induced by LUT@ZIF-8/GelMA hydrogel scaffolds mitigates the adverse effects caused by the inflammatory microenvironment and enhances the osteogenic differentiation of rBMSCs. This aligns with previous studies showing that M2 macrophages secrete cytokines essential for bone formation [11]. Co-culturing MSCs with M2 macrophages has been shown to promote matrix mineralization [73]. As anticipated, in this study, the luteolin and Zn^{2+} released from the LUT@ZIF-8/GelMA hydrogel scaffolds modulate macrophage polarization, fostering an immune microenvironment that supports tissue regeneration.

3.8. *In vivo* assessment of bioprinted scaffolds

In vivo inflammatory regulation and osteogenic properties of the LUT@ZIF-8/GelMA hydrogel scaffolds were evaluated using a rat cranial defect model (Fig. 9A). At 8 weeks post-surgery, cranial samples were harvested for micro-CT scanning to assess bone regeneration (Fig. 9B). Micro-CT imaging revealed that the LUT@ZIF-8/GelMA hydrogel scaffolds induced the most extensive bone regeneration, followed by the LUT/GelMA and ZIF-8/GelMA groups. Minimal bone regeneration was observed in the GelMA group. Quantitative analysis of BV and BV/TV further confirmed these observations, with the LUT@ZIF-8/GelMA group showing significantly higher values compared to all other groups (Fig. 9C–D).

Histological analysis was performed to further assess bone formation (Fig. 10A–B). H&E and Masson's trichrome staining showed that the LUT@ZIF-8/GelMA group demonstrated robust new bone formation in the defect area, whereas the LUT/GelMA, ZIF-8/GelMA, and GelMA groups exhibited limited bone regeneration. In contrast, the Blank group showed minimal new bone formation, with the defect predominantly filled by fibrous tissue. These histological findings correlate with the micro-CT results, reaffirming that the LUT@ZIF-8/GelMA hydrogel scaffold induces the most significant osteogenic effect. Additionally, the hydrogel scaffolds underwent extensive degradation, with only minimal residual hydrogel remaining at the bone defect site, indicating favorable biodegradability *in vivo*. Immunohistochemical staining further evaluated the expression of bone formation markers RUNX2 and OCN. The LUT@ZIF-8/GelMA group significantly elevated RUNX2 and OCN expression levels compared to the other groups (Fig. 10C). These results demonstrate that LUT@ZIF-8/GelMA hydrogel scaffold possesses significant osteogenic potential and effectively promotes bone regeneration.

Recent advances in genetic lineage tracing, flow cytometry, and single-cell analysis have highlighted the complexity and plasticity of macrophage functions, underscoring their critical role in bone remodeling [11,74]. Modulating macrophages at the site of bone defects through biomaterial implantation has emerged as a promising therapeutic strategy [75–77]. Building on the promising osteogenic effects of LUT@ZIF-8/GelMA hydrogel scaffold observed *in vivo*, we next investigated its ability to modulate the immune microenvironment within the bone defect site. To investigate macrophage polarization, IF staining was performed at the early stage of bone regeneration (Fig. S14). In comparison to the Blank group, an increase in iNOS-positive cells was observed in the bone defect region of the GelMA group, indicating a local inflammatory response induced by the implanted material. In contrast, the LUT@ZIF-8/GelMA group showed a reduction in iNOS-positive cells, suggesting an alleviation of the inflammatory response. Furthermore, CD206-positive cells were significantly more abundant in the LUT@ZIF-8/GelMA group compared to both the Blank and GelMA groups, indicating that the LUT@ZIF-8/GelMA hydrogel scaffold promotes M2 macrophage polarization *in vivo*.

The biosafety of LUT@ZIF-8/GelMA hydrogel scaffolds was assessed through histopathological analysis of the rats' vital organs, conducted 8 weeks post-implantation. H&E staining showed no notable adverse effects or organ damage across the experimental groups, in contrast to the Blank group (Fig. S15). These results further confirmed the favorable biosafety profile of the LUT@ZIF-8/GelMA hydrogel, aligning with the *in vitro* toxicity assay outcomes.

In summary, the *in vivo* studies confirmed the dual osteogenic potential and inflammatory regulation of the LUT@ZIF-8/GelMA hydrogel scaffolds. The scaffolds significantly promoted M2 macrophage polarization during the early osteogenic phase, establishing an anti-inflammatory microenvironment conducive to osteogenesis. This inflammatory modulation, combined with the scaffold's osteogenic properties, resulted in enhanced bone formation after 2 months. These findings highlight the potential of LUT@ZIF-8/GelMA hydrogel scaffolds as a promising platform for bone regeneration through the synergistic regulation of osteogenesis and immune response.

Our study demonstrates the great potential of LUT@ZIF-8/GelMA hydrogel scaffolds in bone regeneration; however, the present study is subject to certain limitations. Previous studies have shown that adjusting the composition of the reaction solvent can enhance the drug loading efficiency of luteolin in ZIF-8 nanoparticles [22]. Our current study still has room for further optimization of the reaction conditions to improve the drug loading efficiency. Furthermore, previous studies have demonstrated crosstalk between BMSCs and macrophages, with BMSCs capable of modulating macrophage polarization [78–80]. However, this study did not assess the role of macrophage-BMSC interactions affecting the osteogenic potential of the bioprinted scaffolds, which remains to be explored.

4. Conclusion

In summary, we developed a novel LUT@ZIF-8/GelMA hydrogel scaffold to address the challenges of insufficient endogenous stem cells and the inflammatory microenvironment in bone defects. Functionalized with LUT@ZIF-8 nanoparticles, the hydrogel scaffold enabled the controlled release of luteolin and Zn^{2+}. The LUT@ZIF-8/GelMA

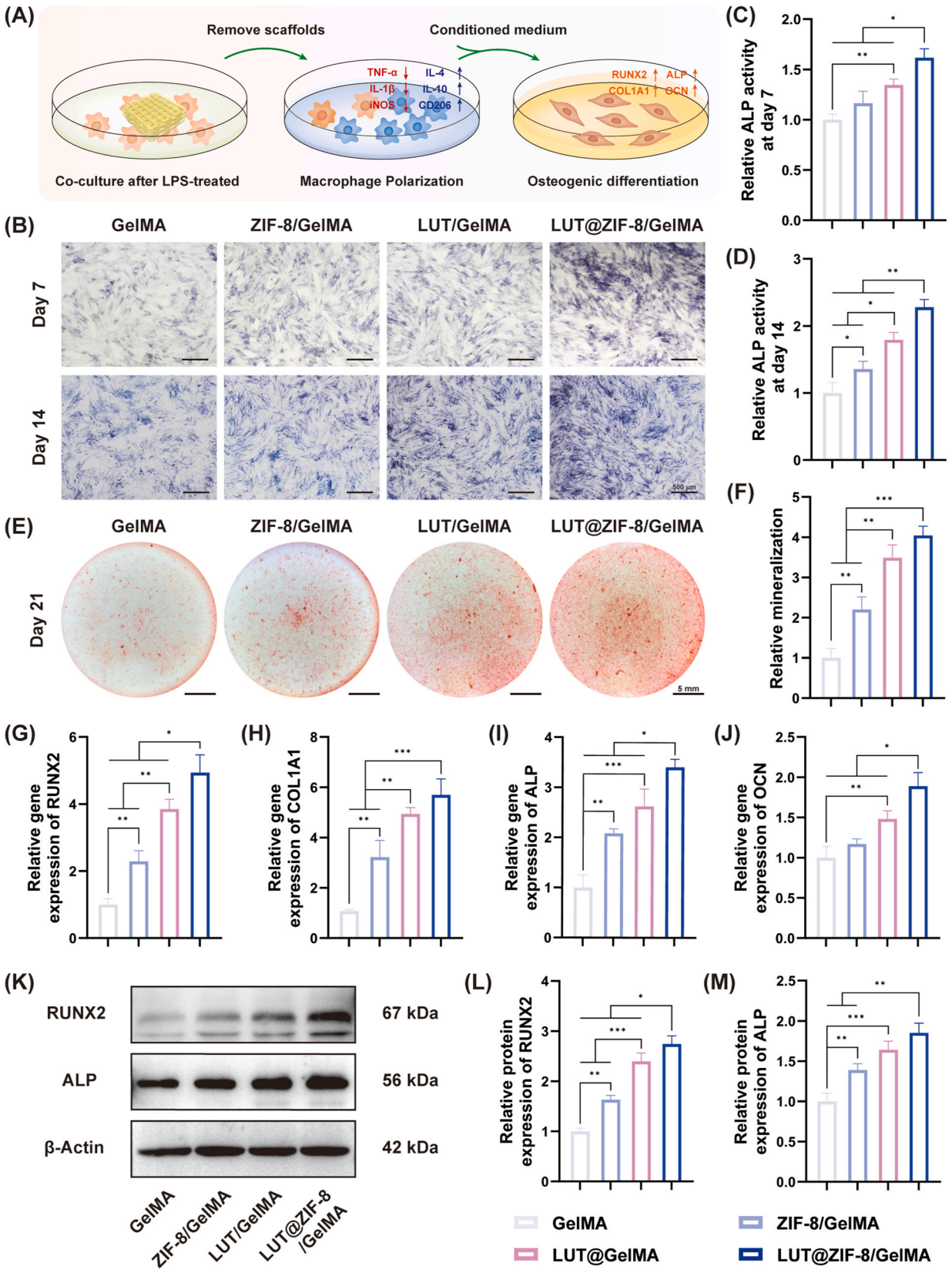

Fig. 8. Osteogenic differentiation mediated by inflammatory regulation. (A) Schematic illustration of osteogenic differentiation induced by conditioned medium. (B) Alkaline phosphatase (ALP) staining after 7 and 14 days of conditioned medium treatment. (C,D) Quantitative analysis of ALP staining. (E,F) Alizarin red S staining and quantitative analysis of mineralization after 21 days of conditioned medium treatment. (G–J) Relative mRNA expression of osteogenesis-related genes after 10 days of conditioned medium treatment. (K) Western blot analysis of osteogenesis-related proteins expression after 10 days of induction. (L,M) Quantification of osteogenesis-related proteins expression levels. (For interpretation of the references to color in this figure legend, the reader is referred to the Web version of this article.)

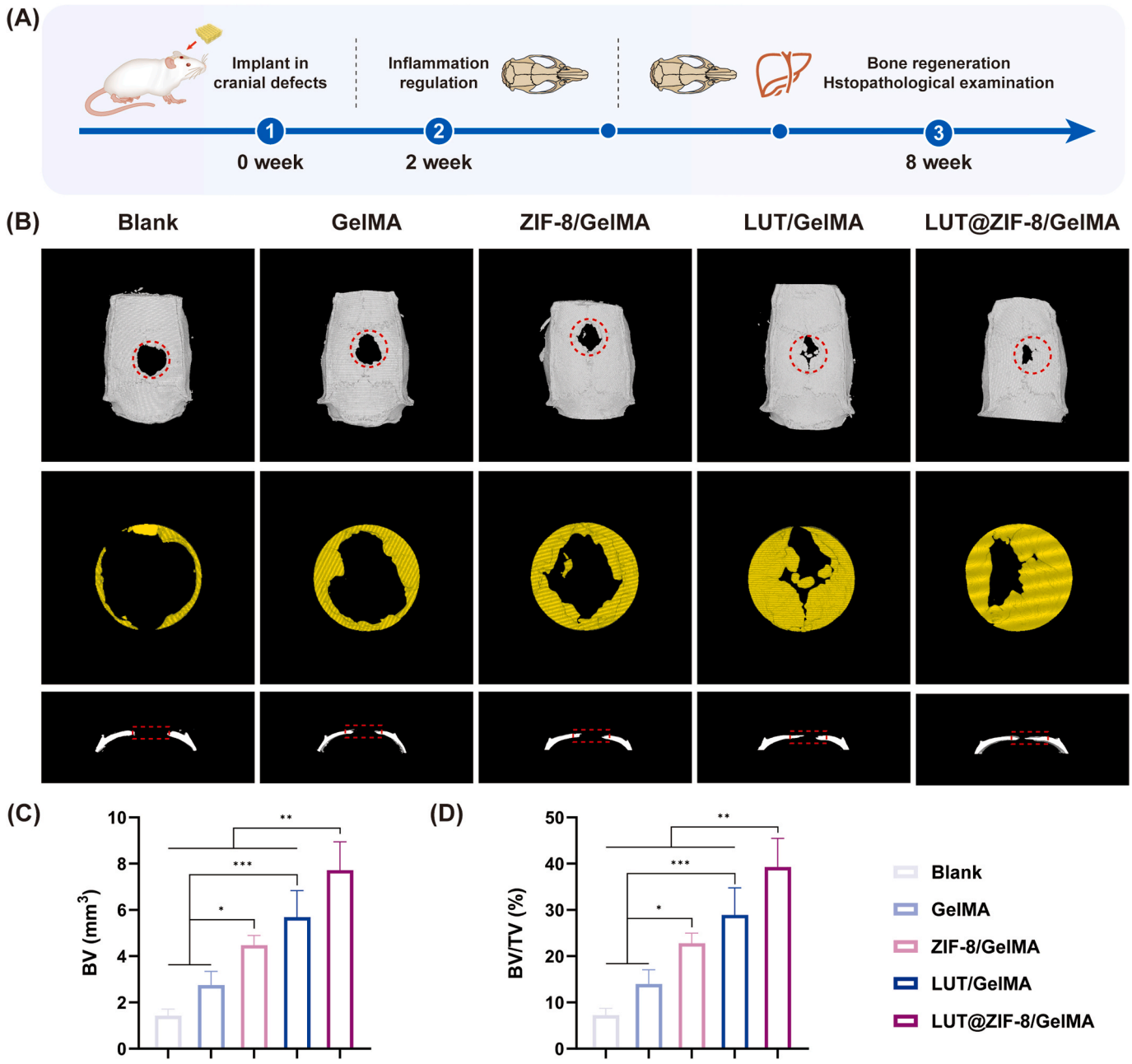

Fig. 9. Evaluation of *in vivo* bone regeneration. (A) Schematic illustration of *in vivo* osteogenic analysis. (B) Micro-CT image of calvarial defects. (C, D) Quantitative analysis of bone volume and percent bone volume.

hydrogel scaffolds exhibited excellent mechanical properties, antibacterial activity, and biocompatibility, significantly enhancing osteogenic differentiation of rBMSCs. Additionally, the LUT@ZIF-8/GelMA hydrogel scaffolds modulated macrophage polarization to create an immune microenvironment conducive to osteogenesis. *In vivo* experiments confirmed that the LUT@ZIF-8/GelMA hydrogel scaffolds effectively promoted bone repair in critical-sized defects. Overall, the LUT@ZIF-8/GelMA hydrogel scaffolds showed excellent bone repair capabilities, presenting a promising approach for bone regeneration.

CRediT authorship contribution statement

San-yang Yu: Writing – original draft, Visualization, Methodology, Investigation, Formal analysis, Data curation, Conceptualization. **Ting Wu:** Validation, Methodology, Investigation, Formal analysis, Data curation. **Kai-hao Xu:** Validation, Project administration, Methodology. **Ru-yue Liu:** Validation, Project administration, Methodology. **Tian-hao Yu:** Writing – review & editing, Resources, Project administration. **Zhen-hua Wang:** Writing – review & editing, Supervision, Resources, Project administration, Funding acquisition. **Zhong-ti Zhang:** Validation, Supervision, Resources, Project administration, Conceptualization.

Funding

This study was supported by the 2023 Liaoning Province Science and Technology Department Special Project to Support the High-quality Development of China Medical University (2023JH2/20200028) and the Liaoning Province Central Government Guiding Local Science and Technology Development Funds (2022JH6/100100058).

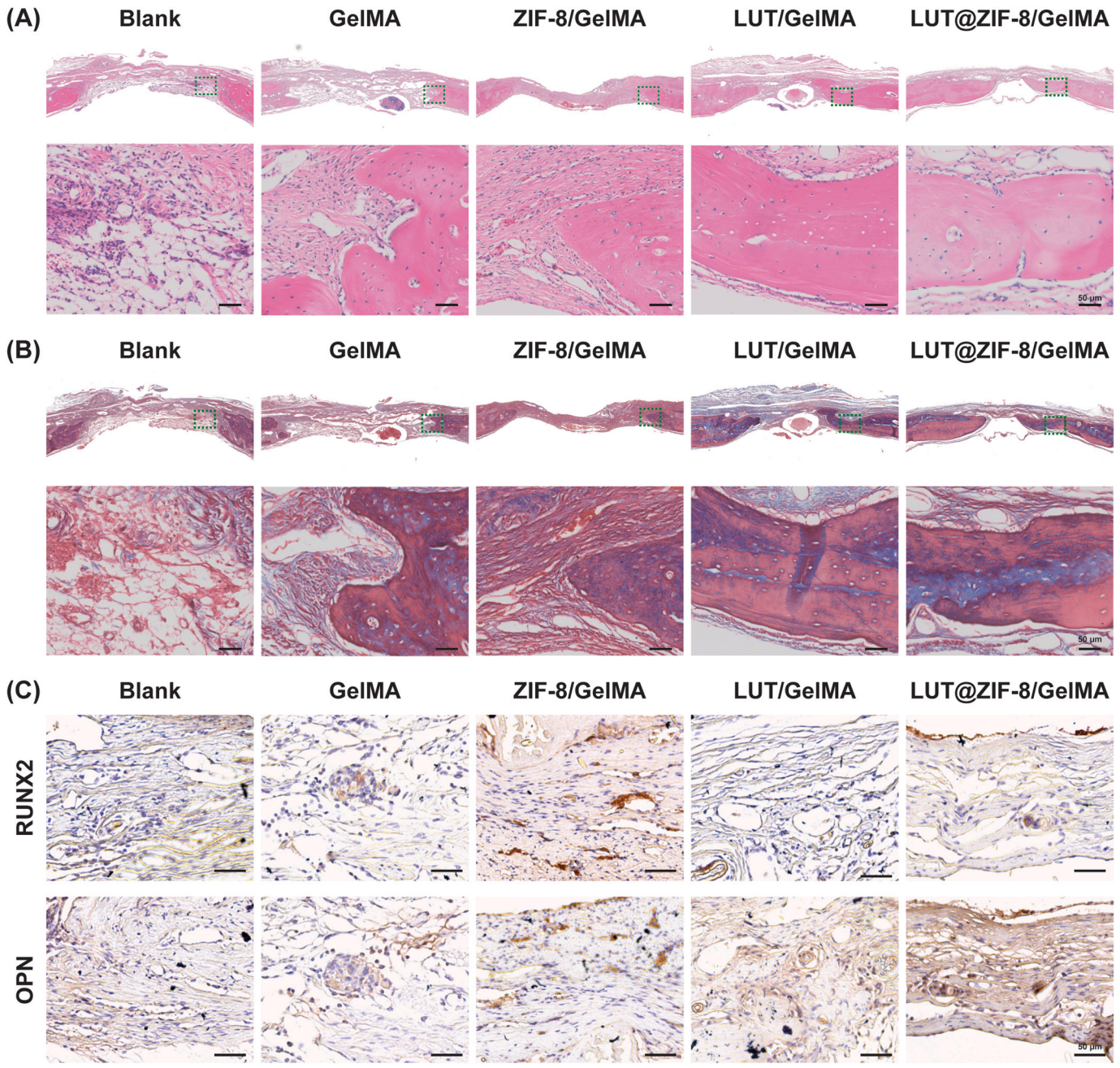

Fig. 10. Histological analysis of bone regeneration. (A) Hematoxylin and eosin staining. (B) Masson's trichrome staining. (C) Immunohistochemistry staining of RUNX2 and OPN.

Declaration of competing interest

The authors declare that they have no known competing financial interests or personal relationships that could have appeared to influence the work reported in this paper.

Appendix A. Supplementary data

Supplementary data to this article can be found online at https://doi.org/10.1016/j.mtbio.2025.101740.

Data availability

Data will be made available on request.

References

[1] R. Dimitriou, E. Jones, D. McGonagle, P.V. Giannoudis, Bone regeneration: current concepts and future directions, BMC Med. 9 (2011) 66, https://doi.org/10.1186/1741-7015-9-66.
[2] N. Su, C. Villicana, D. Barati, P. Freeman, Y. Luo, F. Yang, Stem cell membrane-coated microribbon scaffolds induce regenerative innate and adaptive immune responses in a critical-size cranial bone defect model, Adv. Mater. 35 (2023) e2208781, https://doi.org/10.1002/adma.202208781.
[3] S. Suvarnapathaki, X. Wu, T. Zhang, M.A. Nguyen, A.A. Goulopoulos, B. Wu, G. Camci-Unal, Oxygen generating scaffolds regenerate critical size bone defects, Bioact. Mater. 13 (2022) 64–81, https://doi.org/10.1016/j.bioactmat.2021.11.002.
[4] N. Ashammakhi, A. Hasan, O. Kaarela, B. Byambaa, A. Sheikhi, A.K. Gaharwar, A. Khademhosseini, Advancing frontiers in bone bioprinting, Adv. Healthcare Mater. 8 (2019) e1801048, https://doi.org/10.1002/adhm.201801048.
[5] J. Li, X. Jiang, H. Li, M. Gelinsky, Z. Gu, Tailoring materials for modulation of macrophage fate, Adv. Mater. 33 (2021) e2004172, https://doi.org/10.1002/adma.202004172.

[6] E. Mariani, G. Lisignoli, R.M. Borzì, L. Pulsatelli, Biomaterials: foreign bodies or tuners for the immune response? Int. J. Mol. Sci. 20 (2019) 636, https://doi.org/10.3390/ijms20030636.
[7] R.J. Miron, M. Bohner, Y. Zhang, D.D. Bosshardt, Osteoinduction and osteoimmunology: emerging concepts, Periodontology 94 (2024) (2000) 9–26, https://doi.org/10.1111/prd.12519.
[8] Y. Liu, L. Wang, X. Dou, M. Du, S. Min, B. Zhu, X. Liu, Osteogenesis or apoptosis—twofold effects of Zn2+ on bone marrow mesenchymal stem cells: an in vitro and in vivo study, ACS Omega 9 (2024) 10945–10957, https://doi.org/10.1021/acsomega.3c10344.
[9] D. He, F. Liu, S. Cui, N. Jiang, H. Yu, Y. Zhou, Y. Liu, X. Kou, Mechanical load-induced H2S production by periodontal ligament stem cells activates M1 macrophages to promote bone remodeling and tooth movement via STAT1, Stem Cell Res. Ther. 11 (2020) 112, https://doi.org/10.1186/s13287-020-01607-9.
[10] M. Tsukasaki, H. Takayanagi, Osteoimmunology: evolving concepts in bone–immune interactions in health and disease, Nat. Rev. Immunol. 19 (2019) 626–642, https://doi.org/10.1038/s41577-019-0178-8.
[11] C. Schlundt, H. Fischer, C.H. Bucher, C. Rendenbach, G.N. Duda, K. Schmidt-Bleek, The multifaceted roles of macrophages in bone regeneration: a story of polarization, activation and time, Acta Biomater. 133 (2021) 46–57, https://doi.org/10.1016/j.actbio.2021.04.052.
[12] J. Lee, H. Byun, S.K. Madhurakkat Perikamana, S. Lee, H. Shin, Current advances in immunomodulatory biomaterials for bone regeneration, Adv. Healthcare Mater. 8 (2019) 1801106, https://doi.org/10.1002/adhm.201801106.
[13] Q. Yu, H. Sun, Z. Yue, C. Yu, L. Jiang, X. Dong, M. Yao, M. Shi, L. Liang, Y. Wan, H. Zhang, F. Yao, J. Li, Zwitterionic polysaccharide-based hydrogel dressing as a stem cell carrier to accelerate burn wound healing, Adv. Healthcare Mater. 12 (2023) e2202309, https://doi.org/10.1002/adhm.202202309.
[14] W. Qin, L. Li, W. Niu, W.-R. Wang, D.-W. Wu, C.-G. Song, C.-H. Gao, Z. Mu, F. R. Tay, K. Jiao, L.-N. Niu, Effects of electric field-modulated conductive hydrogel on osseoperception and osseointegration of dental implants, Adv. Funct. Mater. 34 (2024) 2400256, https://doi.org/10.1002/adfm.202400256.
[15] K. Xu, S. Yu, Z. Wang, Z. Zhang, Z. Zhang, Bibliometric and visualized analysis of 3D printing bioink in bone tissue engineering, Front. Bioeng. Biotechnol. 11 (2023), https://doi.org/10.3389/fbioe.2023.1232427.
[16] K. Yue, G.T. Santiago, M.M. Alvarez, A. Tamayol, N. Annabi, A. Khademhosseini, Synthesis, properties, and biomedical applications of gelatin methacryloyl (GelMA) hydrogels, Biomaterials 73 (2015) 254–271, https://doi.org/10.1016/j.biomaterials.2015.08.045.
[17] A.G. Kurian, R.K. Singh, K.D. Patel, J.-H. Lee, H.-W. Kim, Multifunctional GelMA platforms with nanomaterials for advanced tissue therapeutics, Bioact. Mater. 8 (2022) 267–295, https://doi.org/10.1016/j.bioactmat.2021.06.027.
[18] B. Zhou, X. Jiang, X. Zhou, W. Tan, H. Luo, S. Lei, Y. Yang, GelMA-based bioactive hydrogel scaffolds with multiple bone defect repair functions: therapeutic strategies and recent advances, Biomater. Res. 27 (2023) 86, https://doi.org/10.1186/s40824-023-00422-6.
[19] D. Chimene, R. Kaunas, A.K. Gaharwar, Hydrogel bioink reinforcement for additive manufacturing: a focused review of emerging strategies, Adv. Mater. 32 (2020) 1902026, https://doi.org/10.1002/adma.201902026.
[20] M. Zhu, Y. Sun, Y. Su, W. Guan, Y. Wang, J. Han, S. Wang, B. Yang, Q. Wang, H. Kuang, Luteolin: a promising multifunctional natural flavonoid for human diseases, Phytother Res. (2024), https://doi.org/10.1002/ptr.8217.
[21] W. Huang, H. Wu, B. Zheng, Y. Liu, The effects of luteolin on orthodontic tooth movement and relapse, Am. J. Orthod. Dentofacial Orthop. (2024), https://doi.org/10.1016/j.ajodo.2024.09.011.
[22] L. Ding, H. Chen, G. Bi, W. Wang, R. Li, Improved anti-cancer effects of luteolin@ZIF-8 in cervical and prostate cancer cell lines, Heliyon 10 (2024) e28232, https://doi.org/10.1016/j.heliyon.2024.e28232.
[23] Y. Wang, W. Smith, D. Hao, B. He, L. Kong, M1 and M2 macrophage polarization and potentially therapeutic naturally occurring compounds, Int. Immunopharmacol. 70 (2019) 459–466, https://doi.org/10.1016/j.intimp.2019.02.050.
[24] S. Wang, M. Cao, S. Xu, J. Shi, X. Mao, X. Yao, C. Liu, Luteolin alters macrophage polarization to inhibit inflammation, Inflammation 43 (2020) 95–108, https://doi.org/10.1007/s10753-019-01099-7.
[25] M. Çetinkaya, Y. Baran, Therapeutic potential of luteolin on cancer, Vaccines 11 (2023) 554, https://doi.org/10.3390/vaccines11030554.
[26] X. Mi, M. Hu, M. Dong, Z. Yang, X. Zhan, X. Chang, J. Lu, X. Chen, Folic acid decorated zeolitic imidazolate framework (ZIF-8) loaded with baicalin as a nano-drug delivery system for breast cancer therapy, Int. J. Nanomed. 16 (2021) 8337–8352, https://doi.org/10.2147/IJN.S340764.
[27] S. Yu, K. Xu, Z. Wang, Z. Zhang, Z. Zhang, Bibliometric and visualized analysis of metal-organic frameworks in biomedical application, Front. Bioeng. Biotechnol. 11 (2023), https://doi.org/10.3389/fbioe.2023.1190654.
[28] B. Wang, Y. Zeng, S. Liu, M. Zhou, H. Fang, Z. Wang, J. Sun, ZIF-8 induced hydroxyapatite-like crystals enabled superior osteogenic ability of MEW printing PCL scaffolds, J. Nanobiotechnol. 21 (2023) 264, https://doi.org/10.1186/s12951-023-02007-w.
[29] A. Lao, J. Wu, D. Li, A. Shen, Y. Li, Y. Zhuang, K. Lin, J. Wu, J. Liu, Functionalized metal-organic framework-modified hydrogel that breaks the vicious cycle of inflammation and ROS for repairing of diabetic bone defects, Small 19 (2023) e2206919, https://doi.org/10.1002/smll.202206919.
[30] Y. Li, J. Zhu, X. Zhang, Y. Li, S. Zhang, L. Yang, R. Li, Q. Wan, X. Pei, J. Chen, J. Wang, Drug-delivery nanoplatform with synergistic regulation of angiogenesis-osteogenesis coupling for promoting vascularized bone regeneration, ACS Appl. Mater. Interfaces 15 (2023) 17543–17561, https://doi.org/10.1021/acsami.2c23107.
[31] M. Qiao, Z. Xu, X. Pei, Y. Liu, J. Wang, J. Chen, Z. Zhu, Q. Wan, Nano SIM@ZIF-8 modified injectable High-intensity biohydrogel with bidirectional regulation of osteogenesis and Anti-adipogenesis for bone repair, Chem. Eng. J. 434 (2022) 134583, https://doi.org/10.1016/j.cej.2022.134583.
[32] H. Tang, Y. Yu, X. Zhan, Y. Chai, Y. Zheng, Y. Liu, D. Xia, H. Lin, Zeolite imidazolate framework-8 in bone regeneration: a systematic review, J. Contr. Release 365 (2024) 558–582, https://doi.org/10.1016/j.jconrel.2023.11.049.
[33] J. Gao, J. Ren, H. Ye, W. Chu, X. Ding, L. Ding, Y. Fu, Thymosin beta 10 loaded ZIF-8/sericin hydrogel promoting angiogenesis and osteogenesis for bone regeneration, Int. J. Biol. Macromol. 267 (2024) 131562, https://doi.org/10.1016/j.ijbiomac.2024.131562.
[34] A five-in-one novel MOF-modified injectable hydrogel with thermo-sensitive and adhesive properties for promoting alveolar bone repair in periodontitis: antibacterial, hemostasis, immune reprogramming, pro-osteo-/angiogenesis and recruitment, Bioact. Mater. 41 (2024) 239–256, https://doi.org/10.1016/j.bioactmat.2024.07.016.
[35] Hypoxia regulates BG/BMSCs@GelMA bioactive scaffolds to promote angiogenesis, osteogenesis and regulate immune responses for bone regeneration, Chem. Eng. J. 498 (2024) 154879, https://doi.org/10.1016/j.cej.2024.154879.
[36] F. Langenbach, J. Handschel, Effects of dexamethasone, ascorbic acid and β-glycerophosphate on the osteogenic differentiation of stem cells in vitro, Stem Cell Res. Ther. 4 (2013) 117, https://doi.org/10.1186/scrt328.
[37] Synthesis of drug-loaded H-ZIF-8@CaCO3-PEG nanocarrier for synergistic therapy, Inorg. Chem. Commun. 162 (2024) 112225, https://doi.org/10.1016/j.inoche.2024.112225.
[38] V.C. Ramos, C.B.G. Reyes, G.M. García, M.I.S. Quesada, F.J.M.-C. Barrero, J.J. S. Rábago, M.S. Polo, ZIF-8 and its magnetic functionalization as vehicle for the transport and release of ciprofloxacin, Pharmaceutics 14 (2022) 2546, https://doi.org/10.3390/pharmaceutics14112546.
[39] S. Rajhard, L. Hladnik, F.A. Vicente, S. Srčič, M. Grilc, B. Likozar, Solubility of luteolin and other polyphenolic compounds in water, nonpolar, polar aprotic and protic solvents by applying FTIR/HPLC, Processes 9 (2021) 1952, https://doi.org/10.3390/pr9111952.
[40] F. Jia, S. Lin, X. He, J. Zhang, S. Shen, Z. Wang, B. Tang, C. Li, Y. Wu, L. Dong, K. Cheng, W. Weng, Comprehensive evaluation of surface potential characteristics on mesenchymal stem cells' osteogenic differentiation, ACS Appl. Mater. Interfaces (2019), https://doi.org/10.1021/acsami.9b07161.
[41] W.G. Brodbeck, Y. Nakayama, T. Matsuda, E. Colton, N.P. Ziats, J.M. Anderson, Biomaterial surface chemistry dictates adherent monocyte/macrophage cytokine expression in vitro, Cytokine 18 (2002) 311–319, https://doi.org/10.1006/cyto.2002.1048.
[42] N. Li, L. Xie, Y. Wu, Y. Wu, Y. Liu, Y. Gao, J. Yang, X. Zhang, L. Jiang, Dexamethasone-loaded zeolitic imidazolate frameworks nanocomposite hydrogel with antibacterial and anti-inflammatory effects for periodontitis treatment, Materials Today Bio 16 (2022) 100360, https://doi.org/10.1016/j.mtbio.2022.100360.
[43] W. Zhang, H. Liu, L. Yan, X. Mei, Z. Hou, Combining emulsion electrospinning with surface functionalization to fabricate multistructural PLA/CS@ZIF-8 nanofiber membranes toward pH-responsive dual drug delivery, Int. J. Biol. Macromol. 253 (2023) 126506, https://doi.org/10.1016/j.ijbiomac.2023.126506.
[44] J. Yang, Y.S. Zhang, K. Yue, A. Khademhosseini, Cell-laden hydrogels for osteochondral and cartilage tissue engineering, Acta Biomater. 57 (2017) 1–25, https://doi.org/10.1016/j.actbio.2017.01.036.
[45] J.W. Overlin, A.H. Shah, M. Chaubal, K.M. Hotchkiss, R. Olivares-Navarrete, Wnt signaling modulates macrophage polarization and is regulated by biomaterial surface properties, Biomaterials 243 (2020) 119920, https://doi.org/10.1016/j.biomaterials.2020.119920.
[46] Y. Liu, Z. Zhu, X. Pei, X. Zhang, X. Cheng, S. Hu, X. Gao, J. Wang, J. Chen, Q. Wan, ZIF-8-Modified multifunctional bone-adhesive hydrogels promoting angiogenesis and osteogenesis for bone regeneration, ACS Appl. Mater. Interfaces 12 (2020) 36978–36995, https://doi.org/10.1021/acsami.0c12090.
[47] J. Zhu, R.E. Marchant, Design properties of hydrogel tissue-engineering scaffolds, Expet Rev. Med. Dev. 8 (2011) 607–626, https://doi.org/10.1586/erd.11.27.
[48] Z.-Y. Chen, S. Gao, Y.-W. Zhang, R.-B. Zhou, F. Zhou, Antibacterial biomaterials in bone tissue engineering, J. Mater. Chem. B 9 (2021) 2594–2612, https://doi.org/10.1039/D0TB02983A.
[49] X. Niu, S. Xiao, R. Huang, D. Huang, K.E. Aifantis, H. Yu, C. Xue, L. Yin, N. Dunne, X. Li, ZIF-8-modified hydrogel sequentially delivers angiogenic and osteogenic growth factors to accelerate vascularized bone regeneration, J. Contr. Release 374 (2024) 154–170, https://doi.org/10.1016/j.jconrel.2024.08.011.
[50] J. Pasquet, Y. Chevalier, J. Pelletier, E. Couval, D. Bouvier, M.-A. Bolzinger, The contribution of zinc ions to the antimicrobial activity of zinc oxide, Colloids Surf., A 457 (2014) 263–274, https://doi.org/10.1016/j.colsurfa.2014.05.057.
[51] W. Qian, M. Liu, Y. Fu, X. Zhang, Y. Wang, X. Fu, J. Liu, Antimicrobial mechanism of luteolin against staphylococcus aureus and listeria monocytogenes and its antibiofilm properties, Microb. Pathog. 142 (2020) 104056, https://doi.org/10.1016/j.micpath.2020.104056.
[52] Y. Ding, G. Wen, X. Wei, H. Zhou, C. Li, Z. Luo, D. Ou, J. Yang, X. Song, Antibacterial activity and mechanism of luteolin isolated from Lophatherum gracile Brongn. against multidrug-resistant Escherichia coli, Front. Pharmacol. 15 (2024) 1430564, https://doi.org/10.3389/fphar.2024.1430564.
[53] X. Fu, G. Liu, A. Halim, Y. Ju, Q. Luo, G. Song, Mesenchymal stem cell migration and tissue repair, Cells 8 (2019) 784, https://doi.org/10.3390/cells8080784.

[54] N. Rossi, H. Hadad, M. Bejar-Chapa, G.M. Peretti, M.A. Randolph, R.W. Redmond, F.P.S. Guastaldi, BMSCs with tissue-engineered scaffolds for large bone segmental defects, A systematic review (2023), https://doi.org/10.1089/ten.TEB.2022.0213.
[55] T. Osathanon, C.M. Giachelli, M.J. Somerman, Immobilization of alkaline phosphatase on microporous nanofibrous fibrin scaffolds for bone tissue engineering, Biomaterials 30 (2009) 4513–4521, https://doi.org/10.1016/j.biomaterials.2009.05.022.
[56] P. Ramesh, R. Jagadeesan, S. Sekaran, A. Dhanasekaran, S. Vimalraj, Flavonoids: classification, function, and molecular mechanisms involved in bone remodelling, Front. Endocrinol. 12 (2021), https://doi.org/10.3389/fendo.2021.779638.
[57] L.A. Nash, P.J. Sullivan, S.J. Peters, W.E. Ward, Rooibos flavonoids, orientin and luteolin, stimulate mineralization in human osteoblasts through the Wnt pathway, Mol. Nutr. Food Res. 59 (2015) 443–453, https://doi.org/10.1002/mnfr.201400592.
[58] E.-M. Choi, Modulatory effects of luteolin on osteoblastic function and inflammatory mediators in osteoblastic MC3T3-E1 cells, Cell Biol. Int. 31 (2007) 870–877, https://doi.org/10.1016/j.cellbi.2007.01.038.
[59] D. Zhang, Q. Chen, C. Shi, M. Chen, K. Ma, J. Wan, R. Liu, Dealing with the foreign-body response to implanted biomaterials: strategies and applications of new materials, Adv. Funct. Mater. 31 (2021) 2007226, https://doi.org/10.1002/adfm.202007226.
[60] K.E. Martin, A.J. García, Macrophage phenotypes in tissue repair and the foreign body response: implications for biomaterial-based regenerative medicine strategies, Acta Biomater. 133 (2021) 4–16, https://doi.org/10.1016/j.actbio.2021.03.038.
[61] A. Sindrilaru, T. Peters, S. Wieschalka, C. Baican, A. Baican, H. Peter, A. Hainzl, S. Schatz, Y. Qi, A. Schlecht, J.M. Weiss, M. Wlaschek, C. Sunderkötter, K. Scharffetter-Kochanek, An unrestrained proinflammatory M1 macrophage population induced by iron impairs wound healing in humans and mice, J. Clin. Investig. 121 (2011) 985–997, https://doi.org/10.1172/JCI44490.
[62] R.C. Langen, A.M. Schols, M.C. Kelders, E.F. Wouters, Y.M. Janssen-Heininger, Inflammatory cytokines inhibit myogenic differentiation through activation of nuclear factor-kappaB, FASEB J. 15 (2001) 1169–1180, https://doi.org/10.1096/fj.00-0463.
[63] T.A. Wynn, K.M. Vannella, Macrophages in tissue repair, regeneration, and fibrosis, Immunity 44 (2016) 450–462, https://doi.org/10.1016/j.immuni.2016.02.015.
[64] D.P. Vasconcelos, M. Costa, I.F. Amaral, M.A. Barbosa, A.P. Águas, J.N. Barbosa, Modulation of the inflammatory response to chitosan through M2 macrophage polarization using pro-resolution mediators, Biomaterials 37 (2015) 116–123, https://doi.org/10.1016/j.biomaterials.2014.10.035.
[65] R. Klopfleisch, Macrophage reaction against biomaterials in the mouse model – phenotypes, functions and markers, Acta Biomater. 43 (2016) 3–13, https://doi.org/10.1016/j.actbio.2016.07.003.
[66] Y. Hu, L. Tang, Z. Wang, H. Yan, X. Yi, H. Wang, L. Ma, C. Yang, J. Ran, A. Yu, Inducing *in situ* M2 macrophage polarization to promote the repair of bone defects *via* scaffold-mediated sustained delivery of luteolin, J. Contr. Release 365 (2024) 889–904, https://doi.org/10.1016/j.jconrel.2023.11.015.
[67] O.R. Mahon, D.C. Browe, T. Gonzalez-Fernandez, P. Pitacco, I.T. Whelan, S. Von Euw, C. Hobbs, V. Nicolosi, K.T. Cunningham, K.H.G. Mills, D.J. Kelly, A. Dunne, Nano-particle mediated M2 macrophage polarization enhances bone formation and MSC osteogenesis in an IL-10 dependent manner, Biomaterials 239 (2020) 119833, https://doi.org/10.1016/j.biomaterials.2020.119833.
[68] Z. Strizova, I. Benesova, R. Bartolini, R. Novysedlak, E. Cecrdlova, L.K. Foley, I. Striz, M1/M2 macrophages and their overlaps – myth or reality? Clin. Sci. (Lond.) 137 (2023) 1067–1093, https://doi.org/10.1042/CS20220531.
[69] T.-H. Kim, J.W. Jung, B.G. Ha, J.M. Hong, E.K. Park, H.-J. Kim, S.-Y. Kim, The effects of luteolin on osteoclast differentiation, function in vitro and ovariectomy-induced bone loss, J. Nutr. Biochem. 22 (2011) 8–15, https://doi.org/10.1016/j.jnutbio.2009.11.002.
[70] H. Ji, G. Shen, H. Liu, Y. Liu, J. Qian, G. Wan, E. Luo, Biodegradable Zn-2Cu-0.5Zr alloy promotes the bone repair of senile osteoporotic fractures via the immune-modulation of macrophages, Bioact. Mater. 38 (2024) 422–437, https://doi.org/10.1016/j.bioactmat.2024.05.003.
[71] L.J. Raggatt, M.E. Wullschleger, K.A. Alexander, A.C.K. Wu, S.M. Millard, S. Kaur, M.L. Maugham, L.S. Gregory, R. Steck, A.R. Pettit, Fracture healing via periosteal callus formation requires macrophages for both initiation and progression of early endochondral ossification, Am. J. Pathol. 184 (2014) 3192–3204, https://doi.org/10.1016/j.ajpath.2014.08.017.
[72] M.K. Chang, L.-J. Raggatt, K.A. Alexander, J.S. Kuliwaba, N.L. Fazzalari, K. Schroder, E.R. Maylin, V.M. Ripoll, D.A. Hume, A.R. Pettit, Osteal tissue macrophages are intercalated throughout human and mouse bone lining tissues and regulate osteoblast function in vitro and in Vivo1, J. Immunol. 181 (2008) 1232–1244, https://doi.org/10.4049/jimmunol.181.2.1232.
[73] J. Pajarinen, T. Lin, E. Gibon, Y. Kohno, M. Maruyama, K. Nathan, L. Lu, Z. Yao, S. B. Goodman, Mesenchymal stem cell-macrophage crosstalk and bone healing, Biomaterials 196 (2019) 80–89, https://doi.org/10.1016/j.biomaterials.2017.12.025.
[74] A. Shapouri-Moghaddam, S. Mohammadian, H. Vazini, M. Taghadosi, S.-A. Esmaeili, F. Mardani, B. Seifi, A. Mohammadi, J.T. Afshari, A. Sahebkar, Macrophage plasticity, polarization, and function in health and disease, J. Cell. Physiol. 233 (2018) 6425–6440, https://doi.org/10.1002/jcp.26429.
[75] J. Yang, X. Gong, T. Li, Z. Xia, R. He, X. Song, X. Wang, J. Wu, J. Chen, F. Wang, R. Xiong, Y. Lin, G. Chen, L. Yang, K. Cai, Tantalum particles promote M2 macrophage polarization and regulate local bone metabolism via macrophage-derived exosomes influencing the fates of BMSCs, Adv. Healthcare Mater. 13 (2024) e2303814, https://doi.org/10.1002/adhm.202303814.
[76] Y. Yao, X. Cai, F. Ren, Y. Ye, F. Wang, C. Zheng, Y. Qian, M. Zhang, The macrophage-osteoclast Axis in osteoimmunity and osteo-related diseases, Front. Immunol. 12 (2021) 664871, https://doi.org/10.3389/fimmu.2021.664871.
[77] Q. Hu, C.J. Lyon, J.K. Fletcher, W. Tang, M. Wan, T.Y. Hu, Extracellular vesicle activities regulating macrophage- and tissue-mediated injury and repair responses, Acta Pharm. Sin. B 11 (2021) 1493–1512, https://doi.org/10.1016/j.apsb.2020.12.014.
[78] D.-I. Cho, M.R. Kim, H. Jeong, H.C. Jeong, M.H. Jeong, S.H. Yoon, Y.S. Kim, Y. Ahn, Mesenchymal stem cells reciprocally regulate the M1/M2 balance in mouse bone marrow-derived macrophages, Exp. Mol. Med. 46 (2014) e70, https://doi.org/10.1038/emm.2013.135.
[79] S.-J. Zhao, F.-Q. Kong, J. Jie, Q. Li, H. Liu, A.-D. Xu, Y.-Q. Yang, B. Jiang, D.-D. Wang, Z.-Q. Zhou, P.-Y. Tang, J. Chen, Q. Wang, Z. Zhou, Q. Chen, G.-Y. Yin, H.-W. Zhang, J. Fan, Macrophage MSR1 promotes BMSC osteogenic differentiation and M2-like polarization by activating PI3K/AKT/GSK3β/β-catenin pathway, Theranostics 10 (2020) 17–35, https://doi.org/10.7150/thno.36930.
[80] L. Chen, C. Yu, W. Xu, Y. Xiong, P. Cheng, Z. Lin, Z. Zhang, L. Knoedler, A. C. Panayi, S. Knoedler, J. Wang, B. Mi, G. Liu, Dual-targeted nanodiscs revealing the cross-talk between osteogenic differentiation of mesenchymal stem cells and macrophages, ACS Nano 17 (2023) 3153–3167, https://doi.org/10.1021/acsnano.2c12440.